AEM Report Number 2008-1

Venkata Suresh Guthikonda · Ryan S. Elliott

Toward an Effective Interaction Potential Model for the Shape Memory Alloy AuCd

April 2, 2008

Abstract The unusual properties of Shape Memory Alloys (SMAs) result from a lattice level Martensitic Transformation (MT) corresponding to an instability of the SMAs crystal structure. Currently, there exists a shortage of material models that can capture the details of lattice level MTs occurring in SMAs and that can be used for efficient computational investigations of the interaction between MTs and larger-scale features found in typical materials. These larger-scale features could include precipitates, dislocation networks, voids, and even cracks. In this paper, one such model is developed for the SMA AuCd. The model is based on Effective Interaction Potentials (EIPs). That is, atomic interaction potentials that are explicit functions of temperature. In particular, the Morse pair potential is used and its adjustable coefficients are taken to be temperature dependent. A fitting procedure is developed for the EIPs that matches, at a suitable reference temperature, the lattice parameters, instantaneous bulk moduli, thermal expansion coefficients, and heat capacities of FCC Au, HCP Cd, and the B2 cubic austenite phase of the Au-47.5at%Cd alloy. The resulting model is explored using branch-following and bifurcation techniques. A hysteretic temperature-induced MT between the B2 cubic and B19 orthorhombic crystal structures is predicted. The predicted MT is found to have characteristics that compare quite well with the experimentally observed behavior of AuCd SMAs. Unfortunately, the model exhibits an unphysical negative thermal expansion at high temperatures.

Keywords Shape Memory Alloys · Martensitic Transformations · Morse Potential · Material stability · Effective Interaction Potentials · AuCd

PACS 81.30.Kf · 81.30.Hd · 64.60.Cn · 64.70.Kd

1 Introduction

Shape memory alloys (SMAs) are special alloys that exhibit the *shape memory effect* and *pseudo-elasticity*. These peculiar properties are the result of solid-to-solid diffusionless phase transformations that occur in the material. These transformations are called martensitic transformations (MTs) and involve the coordinated motion of atoms in the crystal as the material's structure transitions from one lattice type to another. MTs can be temperature- or stress-induced. The high temperature phase is usually of high symmetry and is called *austenite* and the low temperature phase is usually of low symmetry and is called *martensite*.

The first SMA discovered was AuCd. *Olander* (1932) used electrochemical techniques to identify the B2 cubic (austenite) phase and the B19 orthorhombic (martensite) phase of AuCd. Further, he was the first to recognize its peculiar (i.e., SMA) behavior. Later, *Bystrom and Almin* (1947) performed an

Venkata Suresh Guthikonda · Ryan S. Elliott
Department of Aerospace Engineering and Mechanics, The University of Minnesota,
Minneapolis, MN 55455, USA
E-mail: elliott@aem.umn.edu

X-ray investigation and found the different phases of the AuCd alloy for different compositions. The SMA properties of Au-47.5at%Cd were identified by *Chang and Read* (1951) using an X-ray analysis of the orientation relationships, electrical resistivity measurements, and motion picture studies of the movement of boundaries between the two phases during phase transformation. From the observations of this experiment, it was concluded that Au-47.5at%Cd undergoes a diffusionless transformation from a high symmetry B2 cubic structure to a low symmetry B19 orthorhombic structure when it is cooled to about 60 °C. The reverse transformation occurs from the B19 structure to the B2 structure at 80 °C as the alloy is heated (*Chang and Read*, 1951). The same researchers found the lattice parameters of Au-47.5at%Cd to be: $a = 3.3165$ Å for the B2 cubic structure and $a = 3.1476$ Å, $b = 4.7549$ Å, and $c = 4.8546$ Å for the B19 orthorhombic structure.

Various models have been presented in the literature to simulate the behavior of SMAs. These models can be broadly categorized as continuum mechanics based models, quantum mechanics based Density Functional Theory (DFT) models, and phenomenological atomistic models.

Continuum mechanics based models can be divided into phenomenological and micromechanical type models. Phenomenological models usually consist of a mechanical law to govern the stress-strain behavior and a kinetic law to govern the crystallographic transformation (*Tanaka and Nagaki*, 1982; *Liang and Rogers*, 1990; *Brinson*, 1993; *Ivshin and Pence*, 1994). The mechanical part of the model plays a less significant role and the particular kinetic law distinguishes these models (*Brinson and Huang*, 1996). Micromechanics based models take account of varying amounts of the crystallographic symmetry of SMAs and use the laws of thermodynamics to describe the transformation behavior (*Patoor et al.*, 1988, 1993; *Sun and Hwang*, 1993a,b; *Goo and Lexcellent*, 1997; *Lu and Weng*, 1997; *Huang and Brinson*, 1998; *Vivet and Lexcellent*, 1998; *Shaw*, 2002; *Guthikonda et al.*, 2008). These models use the geometric properties of martensitic variants that make up a transforming inclusion and apply micromechanics calculations to obtain the interaction energy of phase transformation in the material. Stresses and strains are obtained as averages over a volume in which many inclusions may exist. The major shortcoming of these continuum models are that á priori knowledge of the martensite structure must be known. Most of the models rely on the availability of experimentally obtained phase diagrams and other physical properties for both the austenite and martensite phases. In other words, these models can not be used if the nature of the material's MTs are not known. Thus, they are not helpful in the search for new shape memory materials.

Quantum mechanics based first-principles DFT methods are valuable for investigating the energy differences between many phases of a material, and for studying the stability (phonon criterion) of these phases all at 0 K (*Ye et al.*, 1997; *Huang et al.*, 2002; *Parlinski and Parlinska-Wojtan*, 2002; *Huang et al.*, 2003; *Parlinski et al.*, 2003). These methods are capable of calculating atomic-level information regarding energies, forces, and stresses independent of any empirical fitting. DFT calculations such as those of *Huang et al.* (2002, 2003) performed at 0 K show that the B2 cubic austenite crystal structure of NiTi is mechanically unstable. This indicates that temperature effects are responsible for the existence of a stable austenite phase in NiTi at high temperature. However, direct DFT based studies of temperature effects on the microstructural behavior of MTs in NiTi and other SMAs are prohibitive due to the computationally intensive nature of DFT calculations.

In contrast, atomistic models based on Molecular Dynamics (MD) or Monté Carlo (MC) simulations are capable of capturing temperature effects and are invaluable for studying the behavior of homogeneous MTs. In particular, MD simulations based on different phenomenological atomic interaction potentials have been useful for exploring the dependence of a MT on properties such as temperature, composition, concentration of defects, etc. (*Rubini and Ballone*, 1995; *Grujicic and Dang*, 1995; *Shao et al.*, 1996; *Meyer and Entel*, 1998; *Entel et al.*, 1999, 2000; *Ozgen and Adiguzel*, 2003; *Wang et al.*, 2006; *Ishida and Hiwatari*, 2007). However, the extension of MD and MC simulations to larger length- and time-scales in order to study the formation and evolution of microstructures in SMAs is impractical except on the largest of currently available parallel-computing systems. Even on these systems, the size of the simulations of interest would require considerable computation time. Thus, alternative methods need to be developed.

The recent studies of *Elliott et al.* (2006a,b) and *Guthikonda and Elliott* (2008) provide a first step in this direction. In these studies, Effective Interaction Potentials (EIPs) are used to model the behavior of SMAs. That is, atomic interactions are modeled with empirical atomic potentials that are explicit functions of temperature. The EIPs are computationally efficient and capable of capturing a wide range of material behavior. Thus, the EIP methodology appears to be a promising tool for

capturing the real atomic-scale behavior of materials that exhibit MTs while also allowing for the efficient simulation of large-scale phenomena, for example, the formation of complex microstructures. In *Guthikonda and Elliott* (2008) it is observed that an EIP model based on the Morse pair potential is appropriate for capturing a transformation between the B2 cubic structure and the B19 orthorhombic structure. Thus, in this work two EIP models are developed to study the B2 to B19 transformation observed in Au-47.5at%Cd.

The remainder of this paper is organized as follows. Section 2 introduces the EIP model, Cauchy-Born kinematics, the free energy density, equilibrium equations, and the stability criterion that will be used in this work. Thermo-elastic crystal properties of interest are defined in Section 3. Section 4 gives a general description of the approach used to fit the EIP model parameters to experimental data for a binary alloy. In Section 5 a simple model with temperature-dependent pair equilibrium spacing is used to capture the behavior of AuCd. Section 6 discusses the behavior of the model developed in the previous section. It is found that this model does not capture all the desired properties of AuCd. Thus, Section 7 introduces a second EIP model which has temperature-dependent bond-stiffness and pair equilibrium-spacing parameters. Section 8 discusses the behavior of this model, and finally, Section 9 summarizes the results of this work.

2 Effective Interaction Potential model

In this section a model of a perfect, infinite, bi-atomic crystal is presented. First, Section 2.1 discusses the use of an effective pair potential to model the atomic interactions. Second, the kinematics used to describe crystalline deformation are presented in Section 2.2. The focus of this work is to develop a model for the SMA AuCd. This will involve fitting effective interaction potentials to experimentally obtained values for not only the B2 cubic AuCd crystal, but also for pure face-centered cubic (FCC) Au and pure hexagonal-close packed (HCP) Cd crystals. Thus, details of the kinematics for each of these crystal structures are presented. Finally, Section 2.3 defines the crystal's free energy density, its equilibrium equations, and the appropriate stability criteria.

2.1 Effective pair potentials

All materials are made up of atoms. These atoms are attracted to each other by inter-atomic forces. Within the EIP model (*Elliott et al.*, 2006b; *Elliott*, 2008; *Guthikonda and Elliott*, 2008), these forces are derived from empirical potentials. Here, a pair potential $\phi(r;\theta)$ is used, where ϕ is the free energy associated with an interaction between two atoms, r is the distance between two atoms, and $\theta = \frac{T}{T_{\text{ref}}}$ is the non-dimensional temperature with T the absolute temperature and T_{ref} a suitable (but arbitrary) reference temperature. To model a particular material, first a functional form for the pair potential is chosen, such as the well known Lennard-Jones or Morse potential. Next, the interactions between atoms are made temperature-dependent by letting the parameters of the potential be functions of temperature. Finally, any adjustable potential parameters are determined by a fitting procedure in order to match the experimental values of a material's properties.

Multiple types of atoms in a material give rise to multiple types of atomic interactions. For example, a binary alloy such as AuCd is made up of two types of atoms denoted here by "a" (Au) and "b" (Cd) which results in the need for three types of atomic pair interactions $a-a$, $b-b$, and $a-b$. In this case, each of these interactions is modeled with a separate free energy potential denoted by $\phi^{aa}(r;\theta)$, $\phi^{bb}(r;\theta)$, and $\phi^{ab}(r;\theta)$ respectively.

2.2 Cauchy-Born kinematics

In order to describe a perfect infinite crystalline material, a representative translational unit cell is chosen and its associated lattice vectors, $\mathbf{G}_1, \mathbf{G}_2$, and $\mathbf{G}_3$ are identified. The chosen unit cell will contain some number of atoms, N, and the crystal structure is constructed by using the lattice vectors to generate the infinite number of translationally periodic images of the representative unit cell. This is called a "multilattice" description of the crystal structure (*Pitteri and Zanzotto*, 2002).

Deformations of the crystal are described using Cauchy-Born (CB) kinematics (*Huang and Born*, 1962; *Elliott et al.*, 2006a,b). Each unit cell in the crystal is labeled by a set of three integers $\ell = (\ell^1, \ell^2, \ell^3)$ and each atom in a given unit cell is labeled by an integer α. Thus, the reference position of atom α in unit cell ℓ is given by

$$\begin{aligned} \mathbf{X}\left[\begin{smallmatrix}\ell\\ \alpha\end{smallmatrix}\right] &= \mathbf{X}[\ell] + \mathbf{P}[\alpha], \\ \mathbf{X}[\ell] &= \ell^1\mathbf{G}_1 + \ell^2\mathbf{G}_2 + \ell^3\mathbf{G}_3, \end{aligned} \tag{1}$$

where $\mathbf{X}[\ell]$ is the position vector locating unit cell ℓ in space and $\mathbf{P}[\alpha]$ is the relative position vector locating atom α within this unit cell.

As described in *Elliott et al.* (2006b), CB kinematics describe the crystal's deformation in terms of "internal atomic shift vectors" $\mathbf{S}[\alpha]$ and a uniform deformation characterized by a 3×3 symmetric right-stretch tensor $\mathbf{U}$. Thus, the current position of atom α in unit cell ℓ is[1]

$$\mathbf{x}\left[\begin{smallmatrix}\ell\\ \alpha\end{smallmatrix}\right] = \mathbf{U} \cdot (\mathbf{X}\left[\begin{smallmatrix}\ell\\ \alpha\end{smallmatrix}\right] + \mathbf{S}[\alpha]). \tag{2}$$

To eliminate rigid-body translations, $\mathbf{S}[0]$ is set to zero. Rigid-body rotations have already been eliminated by the use of the symmetric right-stretch tensor $\mathbf{U}$, instead of the general 3×3 deformation gradient tensor $\mathbf{F}$.

2.2.1 CB kinematics of the face-centered cubic crystal structure

The face-centered cubic (FCC) crystal has an essential unit cell that contains one atom ($\alpha \in \{0\}$) as shown in Fig. 1. The lattice basis vectors of this unit cell are given by

$$\mathbf{G}_1 = \frac{a_0}{2}(\mathbf{e}_2 + \mathbf{e}_3), \quad \mathbf{G}_2 = \frac{a_0}{2}(\mathbf{e}_3 + \mathbf{e}_1), \quad \mathbf{G}_3 = \frac{a_0}{2}(\mathbf{e}_1 + \mathbf{e}_2), \tag{3}$$

where a_0 is the lattice parameter of the conventional FCC unit cell and $\{\mathbf{e}_1, \mathbf{e}_2, \mathbf{e}_3\}$ is a reference orthonormal basis aligned with the FCC cubic axis. The relative reference position vector locating atom $\alpha = 0$ within the one atom unit cell of the FCC crystal structure is, trivially, taken to be

$$\mathbf{P}[0] = \mathbf{0}. \tag{4}$$

The FCC structure is a Bravais lattice for which the CB kinematics of Eq. (2) simplify to give the current position of each atom in terms of its reference position as

$$\mathbf{x}\left[\begin{smallmatrix}\ell\\ 0\end{smallmatrix}\right] = \mathbf{U} \cdot \mathbf{X}\left[\begin{smallmatrix}\ell\\ 0\end{smallmatrix}\right]. \tag{5}$$

2.2.2 CB kinematics of the hexagonal close-packed crystal structure

The hexagonal close-packed (HCP) crystal structure has an essential unit cell that contains two atoms ($\alpha \in \{0, 1\}$) as shown in Fig. 2. The lattice basis vectors of this unit cell are given by

$$\mathbf{G}_1 = \frac{a_0}{2}(-\mathbf{e}_2 + \sqrt{3}\mathbf{e}_1), \quad \mathbf{G}_2 = a_0\mathbf{e}_2, \quad \mathbf{G}_3 = c_0\mathbf{e}_3, \tag{6}$$

where a_0 and c_0 are the lattice parameters of the HCP crystal and $\{\mathbf{e}_1, \mathbf{e}_2, \mathbf{e}_3\}$ is a reference orthonormal basis as indicated in Fig. 2. The relative reference position vectors locating atoms $\alpha \in \{0, 1\}$ within the two atom unit cell of the HCP crystal structure are taken to be

$$\mathbf{P}[0] = \mathbf{0}, \quad \mathbf{P}[1] = \frac{1}{3}\mathbf{G}_1 + \frac{2}{3}\mathbf{G}_2 + \frac{1}{2}\mathbf{G}_3. \tag{7}$$

2.2.3 CB kinematics of the B2 cubic crystal structure

The B2 cubic crystal structure has an essential unit cell that contains two atoms as shown on the left side of Fig. 3. In this work, a non-essential unit cell containing four atoms (4-lattice) as shown on the right side of Fig. 3 is used in order to capture the crucial deformation modes that determine the stability of the B2 cubic crystal (see *Guthikonda and Elliott*, 2008 for further details).

[1] Here the "Lagrangian" form of CB kinematics is used. Alternative forms are available, however we find this to be the most intuitive representation.

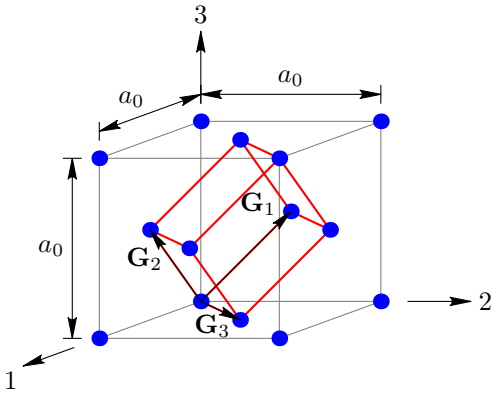

Fig. 1 Conventional unit cell, with four atoms, and essential unit cell, with one atom, of the FCC crystal structure.

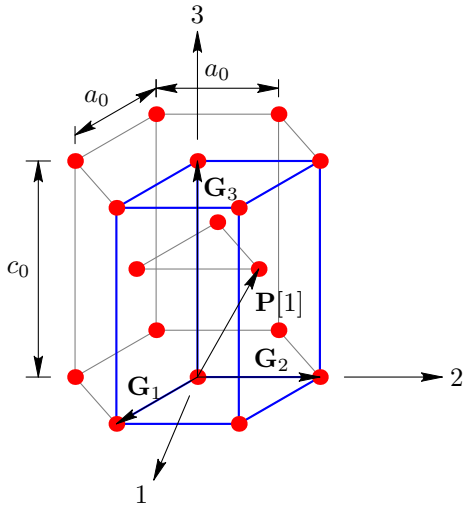

Fig. 2 Conventional unit cell, with six atoms, and essential unit cell, with two atoms, of the HCP crystal structure.

The non-essential lattice vectors, $\mathbf{G}_x, \mathbf{G}_y$, and $\mathbf{G}_z$ are the three non-coplanar vectors for the 4-lattice unit cell. These vectors are related to the essential cubic basis vectors $\mathbf{G}_1 = a_0\mathbf{e}_1, \mathbf{G}_2 = a_0\mathbf{e}_2$, and $\mathbf{G}_3 = a_0\mathbf{e}_3$ (defining the essential unit cell shown on the left side of Fig. 3) by

$$\mathbf{G}_x = \mathbf{G}_1 + \mathbf{G}_2, \quad \mathbf{G}_y = \mathbf{G}_2 - \mathbf{G}_1, \quad \mathbf{G}_z = \mathbf{G}_3. \tag{8}$$

The reference relative position vectors of the four atoms $\alpha \in \{0, 1, 2, 3\}$ for the B2 cubic crystal structure are

$$\begin{aligned} \mathbf{P}[0] &= \mathbf{0}, & \mathbf{P}[1] &= \frac{1}{2}\mathbf{G}_x + \frac{1}{2}\mathbf{G}_z, \\ \mathbf{P}[2] &= \frac{1}{2}\mathbf{G}_x + \frac{1}{2}\mathbf{G}_y, & \mathbf{P}[3] &= \frac{1}{2}\mathbf{G}_y + \frac{1}{2}\mathbf{G}_z, \end{aligned} \tag{9}$$

where $\alpha = 0$ and $\alpha = 2$ correspond to "a" (Au) atoms and $\alpha = 1$ and $\alpha = 3$ correspond to "b" (Cd) atoms as shown in Fig. 3.

2.3 Free energy density, equilibrium equations, and stability criteria

The EIP model gives the crystal's bulk free energy density as half the sum of all effective pair-interactions between atoms in one unit cell, say $\ell = (0, 0, 0)$, and all other atoms in the crystal,

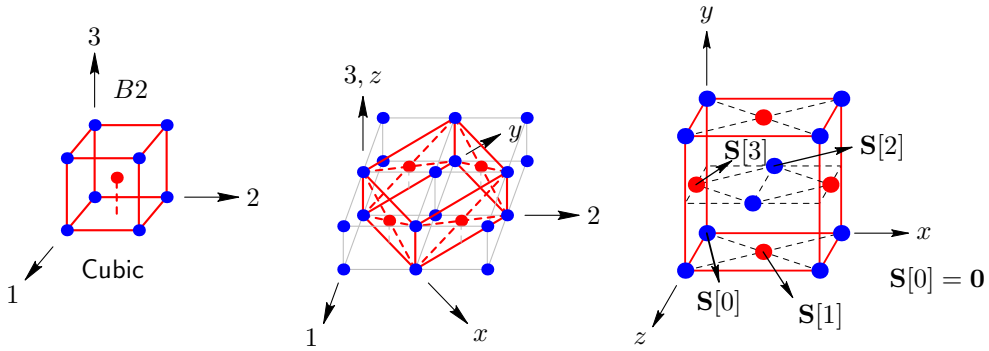

Fig. 3 Essential unit cell (left), with two atoms, and the 4-lattice unit cell used in this work (right), with four atoms, of the B2 cubic crystal structure.

normalized by the reference unit cell volume. Thus, the free energy density per unit reference volume of a crystal is given by

$$\widetilde{W}(\mathbf{u};\theta) = \frac{1}{2V}\sum_{\alpha}\sum_{\left[\substack{\ell'\\ \alpha'}\right]} \phi^{\eta(\alpha)\eta(\alpha')}\left(r\left[\begin{smallmatrix}0\ \ell'\\ \alpha\ \alpha'\end{smallmatrix}\right];\theta\right), \tag{10}$$

where $\mathbf{u} = (\mathbf{U};\mathbf{S}[\alpha])$ represents the chosen set of independent degrees of freedom (DOFs) that describe the deformation of the crystal, θ is the non-dimensional temperature, V is the reference unit cell volume, $\eta(\alpha)$ represents the type of atom α ("a", "b", "c", etc.), and $r\left[\begin{smallmatrix}0\ \ell'\\ \alpha\ \alpha'\end{smallmatrix}\right] \equiv ||\mathbf{x}\left[\begin{smallmatrix}\ell'\\ \alpha'\end{smallmatrix}\right] - \mathbf{x}\left[\begin{smallmatrix}0\\ \alpha\end{smallmatrix}\right]||$ is the current distance between atom α' in unit cell ℓ' and atom α in the unit cell located at the origin. The factor of $1/2$ in Eq. (10) arises from the fact that the summation involves each interaction twice. Technically, the summation over $\left[\begin{smallmatrix}\ell'\\ \alpha'\end{smallmatrix}\right]$ in Eq. (10) extends to all atoms in the infinite crystal, but such a summation is computationally impossible. Due to the rapid decay of most commonly used pair potentials, it is acceptable to employ a cutoff distance r_{cut}. Here r_{cut} is taken as seven atomic distance units, which is found to be sufficient to ensure that the lattice sum in Eq. (10) is converged. Thus, the summation in Eq. (10) extends to all atoms in the Eulerian sphere of influence, that is, all atoms such that $r\left[\begin{smallmatrix}0\ \ell'\\ \alpha\ \alpha'\end{smallmatrix}\right] \leq r_{\text{cut}}$.

The equilibrium equations for the infinite perfect multilattice crystal with zero-stress conditions at infinity are given by the derivatives of $\widetilde{W}$,

$$\frac{\partial\widetilde{W}}{\partial\mathbf{u}} = \mathbf{0}\begin{cases}\frac{\partial\widetilde{W}}{\partial\mathbf{U}} = \mathbf{0},\\ \frac{\partial\widetilde{W}}{\partial\mathbf{S}[\alpha]} = \mathbf{0}, \quad \alpha = 1,2,...,N-1.\end{cases} \tag{11}$$

As shown in *Elliott et al.* (2006a) the translational periodicity of the crystal structure and the use of multilattice CB kinematics ensures that solutions of Eqs. (11) also correspond to true equilibrium configurations for the crystal. That is, if Eqs. (11) are satisfied, then the sum of forces acting on each atom in the crystal is zero.

Due to the "microscopic" nature of the CB shift DOFs, their direct control is difficult if not impossible. Therefore, most available experimental data corresponds to a state of the material in which the shifts are in equilibrium. That is, they satisfy Eq. $(11)_2$ for any given value of the deformation $\mathbf{U}$. Thus, the form of the material's free energy density that is most appropriate for comparison to macroscopic experimental data is the "Homogenized Continuum (HC) free energy density" (*Elliott et al.*, 2006a). To obtain the HC free energy density, Eq. $(11)_2$ is used to implicitly define the shifts $\mathbf{S}[\alpha]$ as functions of the uniform deformation $\mathbf{U}$ and temperature θ, i.e., $\mathbf{S}[\alpha] = \mathbf{S}[\alpha](\mathbf{U};\theta)$. The HC free energy density is then defined by

$$\widetilde{\widetilde{W}}(\mathbf{U};\theta) \equiv \widetilde{W}(\mathbf{U};\mathbf{S}[\alpha](\mathbf{U};\theta);\theta). \tag{12}$$

It is especially important to use the HC free energy density when calculating properties associated with non-centrosymmetric crystals, such as the HCP Bravais lattice and the αIrV and B19 orthorhombic structures encountered in Sections 6 and 8. This is because for these crystals the shifts couple directly to the uniform deformation of the crystal and ignoring this coupling will result in significant errors in the computation of many thermo-elastic material properties. It should be noted that the HC free energy as defined here may not be single valued. That is, for any given deformation $\mathbf{U}$ there may be multiple solutions to Eq. $(11)_2$. These will lead to a multi valued HC free energy. Which of these multiple values $\overset{\approx}{W}(\mathbf{U};\theta)$ takes on at any given time will then depend on the deformation history.

The stability of an equilibrium configuration, i.e., a solution to Eqs. (11), is defined in terms of the "material stability" criterion of *Elliott et al.* (2006b). This requires the crystal to satisfy both the "Cauchy-Born (CB) stability criterion" and the "phonon stability criterion." The CB stability criterion evaluates stability with respect to perturbations of the CB kinematics. The phonon stability criterion evaluates stability with respect to all other bounded perturbations of the equilibrium crystal structure. Together these criteria provide a robust measure of the crystal's stability under soft loading conditions. It is important to note that this stability criterion provides a measure of the crystal's stability that is independent of the particular CB kinematics used to describe the equilibrium crystal structure. Complete definitions and detailed discussions of the CB and phonon stability criteria are given in *Elliott et al.* (2006a) and *Elliott* (2008).

3 Thermo-elastic properties of crystals

In this section, the thermal and elastic material properties that are used in this work for fitting to and comparison with available experimental data are presented.

The cohesive energy E_{c} is the energy (per atom) released by the formation of the crystal from a set of dissociated atoms that are initially infinitely far apart and is given by

$$E_{\mathrm{c}} = -\left(\overset{\approx}{W}(\mathbf{U}_0;\theta_0)\right)\frac{V}{N}, \tag{13}$$

where $\overset{\approx}{W}(\mathbf{U}_0;\theta_0)$ is the HC free energy density, $\mathbf{U}_0$ is the CB deformation corresponding to the stress-free configuration at the non-dimensional temperature θ_0, V is the reference unit cell volume, and N is the number of atoms in the unit cell. The minus sign is required to obtain the energy *released* during the crystal's formation, due to the choice of energy datum corresponding to the dissociated set of atoms.

The entropy per mole S is given by

$$S = -\frac{1}{T_{\mathrm{ref}}}\frac{\partial \overset{\approx}{W}}{\partial \theta}\bigg|_{(\mathbf{U}_0;\theta_0)}\frac{VN_A}{N}, \tag{14}$$

where N_A is Avogadro's constant (6.023×10^{23}).

The thermal expansion tensor $\boldsymbol{\alpha}$ is obtained by taking a total temperature derivative of the stress-free equilibrium equation $\frac{\partial \overset{\approx}{W}}{\partial \mathbf{U}} = \mathbf{0}$, setting $\frac{\partial \mathbf{U}}{\partial \theta} \equiv \boldsymbol{\alpha} T_{\mathrm{ref}}$, and solving for $\boldsymbol{\alpha}$, which results in[2]

$$\boldsymbol{\alpha} = -\frac{1}{T_{\mathrm{ref}}}\left[\left(\frac{\partial^2 \overset{\approx}{W}}{\partial \mathbf{U}^2}\right)^{-1} : \left(\frac{\partial^2 \overset{\approx}{W}}{\partial \mathbf{U}\partial\theta}\right)\right]_{(\mathbf{U}_0;\theta_0)}. \tag{15}$$

For cubic crystals (or isotropic materials), $\boldsymbol{\alpha}$ is an isotropic second-order tensor and one may speak of the "linear thermal expansion coefficient." However, for non-cubic (non-isotropic) materials, the directional dependence of thermal expansion must be specified and, therefore, one speaks of the "thermal expansion tensor."

[2] The double tensor contraction $\mathbf{A} : \mathbf{B}$ is defined in Cartesian tensor component form by $A_{ij}B_{ijkl}$.

The heat capacity per mole at constant volume C_{v} is defined as

$$C_{\mathrm{v}} = -\left(\frac{\theta}{T_{\mathrm{ref}}}\frac{\partial^2 \overset{\approx}{W}}{\partial \theta^2}\right)_{(\mathbf{U}_0;\theta_0)} \frac{VN_A}{N}. \tag{16}$$

The definition of heat capacity per mole at constant pressure is $C_{\mathrm{p}} = T\left(\frac{\partial S}{\partial T}\right)_{\mathrm{p}}$. An expression for C_{p} may be obtained by taking the total derivative of Eq. (14) and multiplying by $T(=\theta\, T_{\mathrm{ref}})$ to obtain

$$C_{\mathrm{p}} = -\left[\frac{\theta}{T_{\mathrm{ref}}}\frac{\partial^2 \overset{\approx}{W}}{\partial \theta^2} + \theta \frac{\partial^2 \overset{\approx}{W}}{\partial \theta \partial \mathbf{U}} : \boldsymbol{\alpha}\right]_{(\mathbf{U}_0;\theta_0)} \frac{VN_A}{N}, \tag{17}$$

where $\boldsymbol{\alpha}$ is the thermal expansion tensor of Eq. (15).

The instantaneous second-order elastic moduli may be obtained by defining a new energy density with reference configuration taken as the current configuration, $\overset{\approx}{W}{}^*(\mathbf{U}^*;\theta) \equiv \overset{\approx}{W}(\mathbf{U}^* \cdot \mathbf{U}_0;\theta)/\det(\mathbf{U}_0)$. The instantaneous moduli are,

$$\begin{aligned}
\mathcal{L}_{ijkl} &= \frac{\partial^2 \overset{\approx}{W}{}^*}{\partial U^*_{ij} \partial U^*_{kl}} \\
&= \frac{1}{4\,\det(\mathbf{U}_0)}\left[U_{0iq}\frac{\partial^2 \overset{\approx}{W}}{\partial U_{qj}\partial U_{ks}}U_{0sl} + U_{0iq}\frac{\partial^2 \overset{\approx}{W}}{\partial U_{qj}\partial U_{ls}}U_{0sk} + \right. \\
&\qquad \left. U_{0jq}\frac{\partial^2 \overset{\approx}{W}}{\partial U_{qi}\partial U_{ks}}U_{0sl} + U_{0jq}\frac{\partial^2 \overset{\approx}{W}}{\partial U_{qi}\partial U_{ls}}U_{0sk}\right].
\end{aligned} \tag{18}$$

The instantaneous bulk modulus K for the material relates a change in volume to an increment in an applied hydrostatic pressure. In terms of the instantaneous moduli $\boldsymbol{\mathcal{L}}$, the instantaneous bulk modulus is

$$K = 1 \Big/ 3\ \left[\mathbf{P} : \boldsymbol{\mathcal{L}}^{-1} : \mathbf{P}\right]_{(\mathbf{U}_0;\theta_0)}, \tag{19}$$

where $\mathbf{P} = \frac{1}{\sqrt{3}}\mathbf{I}$ represents a "unit pressure." It is worth noting that some authors define the instantaneous bulk modulus as the proportionality constant relating a change in the spherical part of the stress to an increment of an applied pure dilatation. This results in an instantaneous bulk modulus defined as

$$K = \frac{1}{3}\left[\boldsymbol{\epsilon} : \boldsymbol{\mathcal{L}} : \boldsymbol{\epsilon}\right]_{(\mathbf{U}_0;\theta_0)}, \tag{20}$$

where $\boldsymbol{\epsilon} = \frac{1}{\sqrt{3}}\mathbf{I}$ represents a "unit dilation."

The two definitions, Eq. (19) and Eq. (20), are in general, different. In the special case of a cubic crystal or an isotropic material they agree but otherwise significant discrepancies occur[3]. Therefore, one must use special care to determine which definition has been used when experimental data is reported in the literature. We feel that Eq. (19) more accurately represents the common interpretation of the instantaneous bulk modulus. Therefore, Eq. (19) will be used exclusively in the remainder of this work.

[3] For example, the instantaneous bulk modulus of HCP Cd (*Fast et al.*, 1995) is $K = 58.13$ GPa when Eq. (20) is used. However, a value 16.77% smaller, $K = 48.38$ GPa, is found when Eq. (19) is used.

4 General approach to fitting model parameters

Once a specific EIP model has been adopted (as discussed in Section 2.1), the adjustable potential parameters of the model must be determined in order to implement the model, as described in Sections 2.2 and 2.3, and to study the material's SMA properties. The approach used in this work to determine these parameters starts by choosing a reference temperature for which significant experimental data is available for the alloy of interest. Next, the properties of the individual bond types are fit to their corresponding elemental material properties. For example, the properties of Au at the reference temperature are used in order to determine the adjustable potential parameters associated with interactions of two Au atoms. Finally, the unlike bond parameters are fit so that the B2 austenite structure's properties match the experimental data for the SMA at the reference temperature.

In this way, all of the model's behavior is determined in terms of the pure elemental properties and the properties of the alloy at high temperature in the austenite phase. Note that this procedure does not use any information about the martensite phase of the material. Thus, the properties of, and even the existence of, the martensite phase are determined by the physics of the particular EIP model under consideration. In particular, the relative properties of the like bonds, which are fit to independent experimental data, provide a realistic setting that will either favor or disfavor the existence of a transformation. Thus, the success of any particular model will be evaluated based on the model's prediction of the correct MT and its associated properties. This includes the model's ability to capture the correct martensite crystal structure, the structure's lattice parameters, and quantities like the latent heat of transformation.

Many alternative fitting procedures are possible. For instance, one could fit all of the model's parameters (for both like and unlike bonds) to an extensive set of experimental data for the alloy. This would, undoubtedly, provide a model that matches the alloy's observed mechanical and thermal behavior more closely than the ones developed in this work. Here, however, we prefer the above described procedure because of its ability to explore the relationship between the constituent element's behavior and the alloy's MT behavior.

5 Model 1: Morse EIPs with temperature-dependent pair equilibrium spacing

The EIP model of *Elliott et al.* (2006b) is adapted to study the binary alloy Au-47.5at%Cd. This model uses temperature-dependent Morse pair potentials. The pair equilibrium spacing $\hat{r}(\theta)$ of the potential is taken to be a linear function of temperature and all other parameters are independent of temperature. Thus, the three Morse potentials which account for the three types of interactions present in the binary alloy take the general form

$$\begin{aligned} \phi(r;\theta) &= A\left\{\exp\left[-2B\left(\frac{r}{\hat{r}(\theta)}-1\right)\right]-2\exp\left[-B\left(\frac{r}{\hat{r}(\theta)}-1\right)\right]\right\}, \\ \hat{r}(\theta) &= r_{\text{ref}}+r_\theta(\theta-1). \end{aligned} \tag{21}$$

The parameters r_{ref} and r_θ are constants that describe the linear variation of $\hat{r}$ with θ. Thus, the model has 12 parameters, four per bond type, that will be fit to the experimental data for pure Au, pure Cd, and B2 AuCd. A reference temperature of $T_{\text{ref}} = 323$ K is used. This is an arbitrary, but convenient choice corresponding to the experimentally observed transformation temperature of Au-47.5at%Cd (*Zirinsky*, 1956).

In *Guthikonda* (2007), an attempt to determine the potential parameters was made by fitting experimental values of the lattice parameters and two elastic moduli for Au, Cd, and AuCd at the reference temperature. For this temperature ($\theta = 1$) the three parameters A, B, and r_{ref} must be determined for each bond type. Note that the parameter r_θ becomes insignificant at $\theta = 1$. Lattice parameters and elastic moduli were chosen for fitting due to their significant role in MTs. Fitting the experimental values of lattice parameters is important due to the crucial role that geometric compatibility is known to play in the formation of microstructure during MT (*Bhattacharya*, 2003). Additionally, since MTs result from lattice instabilities it seemed sensible to regard the material's elastic moduli, which are the indicators of stability, as important quantities to match as well.

Unfortunately, it was determined that a fitting procedure for the effective Morse pair potentials that matches the lattice parameters and two elastic moduli of the material of interest is not possible.

See *Guthikonda* (2007) for a detailed discussion. Thus, a more generalized procedure is adapted to determine the adjustable parameters by fitting the experimental values of lattice parameter, instantaneous bulk modulus, and cohesive energy. This procedure follows that of *Girifalco and Weizer* (1959) who fit the Morse potential for a number of cubic pure elements. They did not, however, consider alloys or temperature-dependent potentials as considered here. The fitting procedure first determines the like-interaction potential parameters from the properties of the corresponding pure materials and finally determines the unlike-interaction potential parameters from the properties of B2 AuCd at the reference temperature.

5.1 Fitting of potential parameters for Au-Au interactions

The pure Au bond parameters $A^{aa}, B^{aa}, r_{\text{ref}}^{aa}$, and r_θ^{aa} are determined by fitting the stress-free equilibrium FCC lattice spacing a, instantaneous bulk modulus K, cohesive energy E_{c}, and linear thermal expansion coefficient α at the reference temperature. A simple trial and error approach was used to match these parameters to the experimental values of FCC Au given in Table 1.

FCC Au at T=323 K

Property	Value
Lattice parameter (a)	4.0812 Å
Bulk modulus (K)	172.2 GPa
Cohesive energy (E_{c})	3.81 $\frac{\text{eV}}{\text{atom}}$
Linear thermal expansion coefficient (α)	14.24×10^{-6} K^{-1}

Table 1 Experimental values of lattice parameter a, instantaneous bulk modulus K, cohesive energy E_{c}, and linear thermal expansion coefficient α for FCC Au at 323 K (*Villars et al.*, 1985; *Neighbours and Alers*, 1958; *Kittel*, 2005).

The fitted parameters for the effective Morse potential for pure Au, $\phi^{aa}(r;\theta)$, are given in Table 2. Figure 4 shows the variation of lattice parameter and instantaneous bulk modulus of FCC Au with

Parameter	Value
A^{aa}	0.4754131760 eV
B^{aa}	4.7788992600
r_{ref}^{aa}	3.0284951200 Å
r_θ^{aa}	0.0139252220 Å

Table 2 Fitted parameters for the effective Morse potential for pure Au, $\phi^{aa}(r;\theta)$.

respect to θ for the resulting potential. It is recognized that negative values of θ are not physical, but the full diagrams are presented for consistency with the figures of Section 6 and so that the model's complete range of behavior is illustrated. The plus sign in each plot shows the corresponding experimental value given in Table 1. At the reference temperature, the cohesive energy of the fitted potential is equal to the experimental value given in Table 1. As θ varies, E_{c} changes negligibly due to a weak dependence on temperature resulting from the small value of r_θ^{aa}. Finally, it can be shown that, for the potential of Eq. (21), the linear thermal expansion coefficient of a Bravais lattice is constant. For the potential defined by the parameters in Table 2, the linear thermal expansion coefficient matches that of FCC Au given in Table 1.

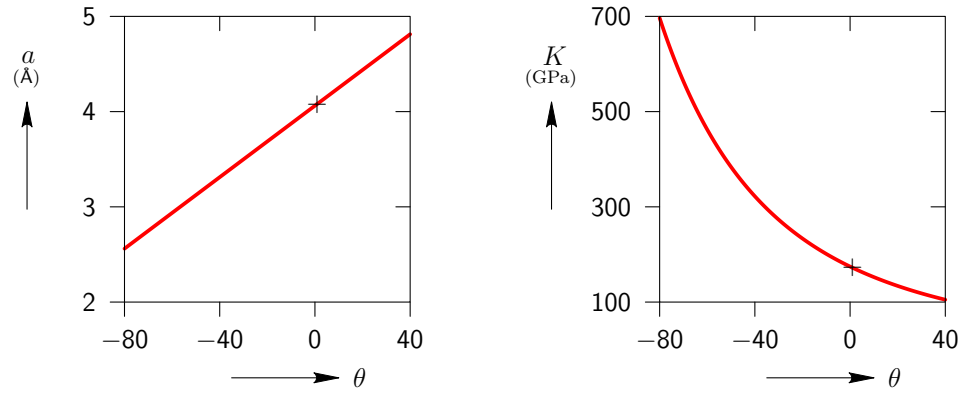

Fig. 4 Variation of lattice parameter a and instantaneous bulk modulus K of FCC Au with respect to the non-dimensional temperature θ for the parameters in Table 2. Plus signs identify the corresponding experimental values at the reference temperature $\theta = 1$.

5.2 Fitting of potential parameters for Cd-Cd interactions

A similar procedure is used to match the experimental values of the HCP close-packed plane lattice parameter, instantaneous bulk modulus, cohesive energy, and the in-plane linear thermal expansion coefficient. The experimental values are given in Table 3. The resulting parameters of the Cd interaction potential, $\phi^{bb}(r;\theta)$, are given in Table 4.

HCP Cd at T=323 K

Property	Value
Lattice parameter (a)	2.9751 Å
Bulk modulus (K)	48.38 GPa
Cohesive energy (E_c)	1.16 $\frac{\text{eV}}{\text{atom}}$
Thermal expansion coefficient (α)	22.1 $\times$ 10^{-6} K^{-1}

Table 3 Experimental values of lattice parameter a, instantaneous bulk modulus K, cohesive energy E_c, and in-plane linear thermal expansion coefficient α at 323 K (*Garland and Silverman*, 1960; *Kittel*, 2005; *Villars et al.*, 1985).

Parameter	Value
A^{bb}	0.1450200350 eV
B^{bb}	4.8068349900
r^{bb}_{ref}	3.1179265800 Å
r^{bb}_{θ}	0.0300213183 Å

Table 4 Fitted parameters for the effective Morse potential for pure Cd, $\phi^{bb}(r;\theta)$.

Figure 5 shows the variation of the lattice parameter a and instantaneous bulk modulus K of HCP Cd with respect to θ for the fitted parameters in Table 4. The plus sign in each plot shows the experimental value given in Table 3. At the reference temperature, the cohesive energy of the fitted potential is equal to the experimental value given in Table 4. As θ varies, E_c changes negligibly due to a weak dependence on temperature resulting from the small value of r^{bb}_{θ}. Similar to the case of Au, the thermal expansion tensor is constant and equal to the value given in Table 4.

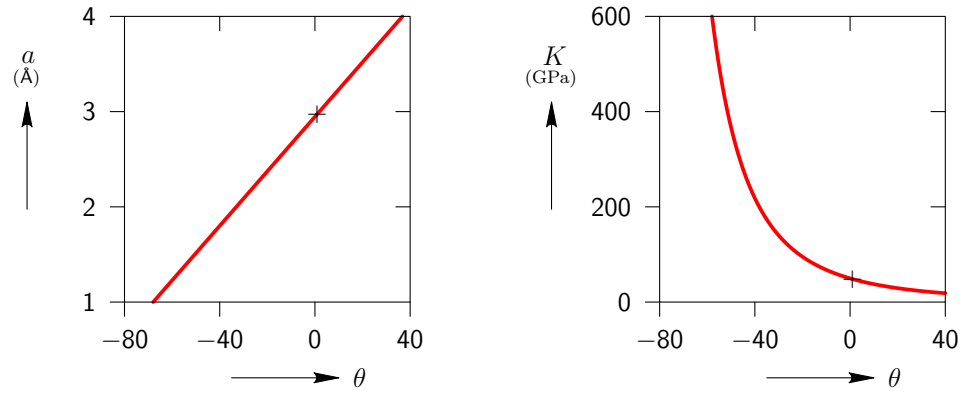

Fig. 5 Variation of lattice parameter a and instantaneous bulk modulus K of HCP Cd with respect to the non-dimensional temperature θ for the parameters in Table 4. Plus signs identify the corresponding experimental values at the reference temperature $\theta = 1$.

5.3 Fitting of potential parameters for Au-Cd interactions

The unlike bond parameters are fit with a procedure similar to that used for the like bond interactions. The experimental values of lattice parameter, instantaneous bulk modulus, cohesive energy, and linear thermal expansion coefficient of the B2 crystal structure of Au-47.5at%Cd at the reference temperature are given in Table 5. Unfortunately, the potential parameters found by fitting to the values in Table 5 result in a model for which the B2 structure is always unstable within a reasonable temperature range. To address this short coming, the fitting procedure is modified.

B2 AuCd at T=323 K

Property	Value
Lattice parameter (a)	3.3165 Å
Bulk modulus (K)	95.78 GPa
Cohesive energy (E_c)	2.6936473 $\frac{\text{eV}}{\text{atom}}$
Thermal expansion coefficient (α)	20.9×10^{-6} K^{-1}

Table 5 Experimental values of lattice parameter a, instantaneous bulk modulus K, cohesive energy E_c, and linear thermal expansion coefficient α of B2 AuCd at 323 K (*Chang and Read*, 1951; *Zirinsky*, 1956; *McGilip*, 1987).

Since lattice parameter and elastic constant play an important role during MT, the fitting of lattice parameter and bulk modulus are retained. The matching of cohesive energy for the unlike bond interaction is replaced by requiring that the B2 alloy be at its stability transition point at the reference temperature. This is appropriate because the reference temperature is chosen as the experimentally observed transformation temperature of Au-47.5at%Cd. The like bond parameters remain as found in Sections 5.1 and 5.2. The complete set of 12 parameters for the three Morse potentials of the EIP model of Eq. (21) is given in Table 6. Figure 6 shows the variation of lattice parameter, instantaneous bulk modulus, cohesive energy, and linear thermal expansion coefficient of B2 AuCd with non-dimensional temperature θ. Plus signs show the corresponding experimental values from Table 5. Note that the experimental cohesive energy E_c is not matched at the reference temperature.

6 Temperature induced MTs associated with Model 1

In order to evaluate the EIP model for AuCd developed in the previous section, its stress-free bifurcation diagram is generated with the non-dimensionalized temperature θ serving as loading parameter. The

techniques of *Elliott et al.* (2002a,b, 2006a,b) are used to identify bifurcation points and emerging bifurcated equilibrium paths. Figure 7 displays the results by plotting the maximum principal stretch λ_3 (largest eigenvalue of the right stretch tensor $\mathbf{U}$) vs. the non-dimensional temperature θ. The B2 austenite phase (red line) changes stability at $\theta = 1$ (by construction) and a set of equilibrium paths emerge from this bifurcation point which correspond to B19 and αIrV type crystal structures (see *U.S. NRL Center for Computational Materials Science*, 2008). In the bifurcation diagram, unstable path segments are represented by dashed lines and stable (CB and phonon) path segments are represented by solid lines. Bifurcation points are shown by open circles and turning points by solid circles on the equilibrium paths. After emerging from the bifurcation point at $\theta = 1$, the B19 equilibrium path (green line) becomes stable as it crosses a turning point near $\theta = 32$ and continues to be stable until it encounters a bifurcation point near $\theta = -20$. Ultimately, the B19 equilibrium path reconnects with the B2 path at a bifurcation point near $\theta = -13$. Similarly, the αIrV equilibrium path (purple line) emerges from the B2 bifurcation point, traverses a turning point, and then becomes stable at the bifurcation point near $\theta = -1$. It continues to be stable until it reaches a turning point at a temperature near $\theta = -65$. Finally, the αIrV path reconnects with the B2 path at the same point as the B19 path. The bifurcation points on the B19 and αIrV paths are connected by unstable monoclinic paths that have space group symmetry P2/m (yellow line). The existence of a stable B19 phase at the reference temperature ($\theta = 1$) indicates the possibility of a MT between the B2 and B19 structures. The associated transformation stretch tensor $\mathbf{U}^*$ for the current model is found to be

$$\mathbf{U}^* = \begin{pmatrix} 1.05451615 & 0.02919474 & 0 \\ 0.02919474 & 1.05451615 & 0 \\ 0 & 0 & 0.89921453 \end{pmatrix}, \tag{22}$$

where $\mathbf{U}_{\mathrm{B19}} = \mathbf{U}^* \cdot \mathbf{U}_{\mathrm{B2}}$. Here, $\mathbf{U}_{\mathrm{B19}}$ is the Right Stretch tensor for the stress-free configuration of the B19 orthorhombic structure at the reference temperature ($\theta = 1$), and $\mathbf{U}_{\mathrm{B2}}$ is the Right Stretch tensor of the stress-free B2 cubic structure at $\theta = 1$. The components of $\mathbf{U}^*$ are given in an ortho-normal basis aligned with the reference B2 cubic axes. The corresponding experimental value (*Ohba et al.*, 1990) is

$$\mathbf{U}^*_{\mathrm{exp}} = \begin{pmatrix} 1.0260 & 0.0100 & 0 \\ 0.0100 & 1.0260 & 0 \\ 0 & 0 & 0.9501 \end{pmatrix}. \tag{23}$$

There is reasonable agreement between the EIP model's prediction and the experimentally observed value of the transformation stretch tensor.

Model 1

Parameter	Value
A^{aa}	0.4754131760 eV
B^{aa}	4.7788992600
r^{aa}_{ref}	3.0284951200 Å
r^{aa}_{θ}	0.0139252220 Å
A^{bb}	0.1450200350 eV
B^{bb}	4.8068349900
r^{bb}_{ref}	3.1179265800 Å
r^{bb}_{θ}	0.0300213183 Å
A^{ab}	0.1426239530 eV
B^{ab}	6.0000000000
r^{ab}_{ref}	3.0855868000 Å
r^{ab}_{θ}	0.0205887304 Å

Table 6 Fitted parameters for the Morse EIP Model 1 of Au-47.5at%Cd.

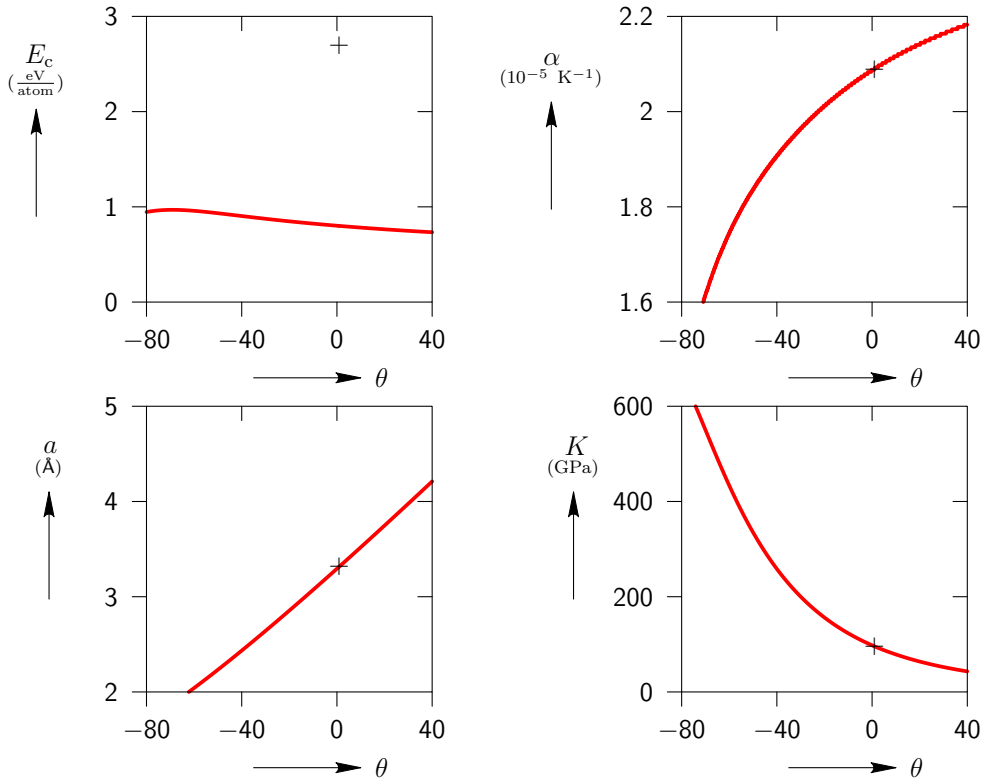

Fig. 6 Variation of cohesive energy E_c, linear thermal expansion coefficient α, lattice parameter a, and instantaneous bulk modulus K of B2 Au-47.5at%Cd with non-dimensional temperature θ for the parameters in Table 6. Plus signs identify the corresponding experimental values at the reference temperature $\theta = 1$.

The variation of the HC free energy density with θ is shown in Fig. 8. This plot reveals a couple of problems with the current model for AuCd. First, the B19 phase is found to be stable for a wide range of temperatures. This implies too large of a temperature hysteresis for the B2 $\leftrightarrow$ B19 MT. Second, these stress-free free energy vs. temperature curves should be interpreted as the Gibbs free-energy density of the material (variation of energy with temperature under constant stress conditions). Under this interpretation, one may immediately note that the model predicts negative values of both entropy (corresponding to the negative of the slope of the curves in Fig. 8, and defined by Eq. (14)) and heat capacity at constant pressure (proportional to the second derivative of the curves in Fig. 8, and defined by Eq. (17)). This is further illustrated in Fig. 9 and Fig. 10, which plot the entropy per mole and heat capacity per mole at constant pressure vs. θ respectively. The basic laws of equilibrium thermodynamics dictate that these quantities must be positive for a stable material. It is therefore concluded that the EIP model, characterized by Eq. (21), is not capable of accurately predicting both the mechanical and thermal properties of the SMA Au-47.5at%Cd. The next section of this work introduces a more general form of the Morse EIP model that is capable of more accurately capturing these properties.

7 Model 2: Morse EIPs with temperature-dependent bond stiffness and pair equilibrium spacing

The effective Morse pair potential is now extended to include a linear temperature dependence of the bond stiffness parameter B giving

$$\begin{aligned}\phi(r;\theta) &= A\left\{\exp\left[-2B(\theta)\left(\frac{r}{\hat{r}(\theta)}-1\right)\right]-2\exp\left[-B(\theta)\left(\frac{r}{\hat{r}(\theta)}-1\right)\right]\right\},\\ \hat{r}(\theta) &= r_{\text{ref}}+r_\theta(\theta-1),\\ B(\theta) &= B_{\text{ref}}+B_\theta(\theta-1).\end{aligned} \tag{24}$$

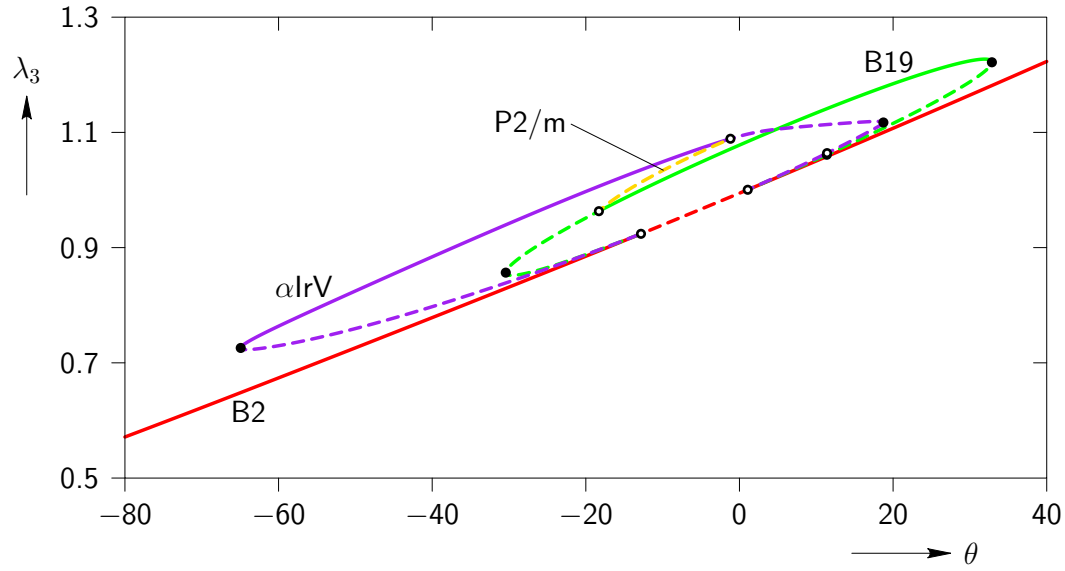

Fig. 7 Variation of λ_3 (largest eigenvalue of $\mathbf{U}$) for the stress-free B2, B19, αIrV, and P2/m crystal structures with respect to non-dimensional temperature θ.

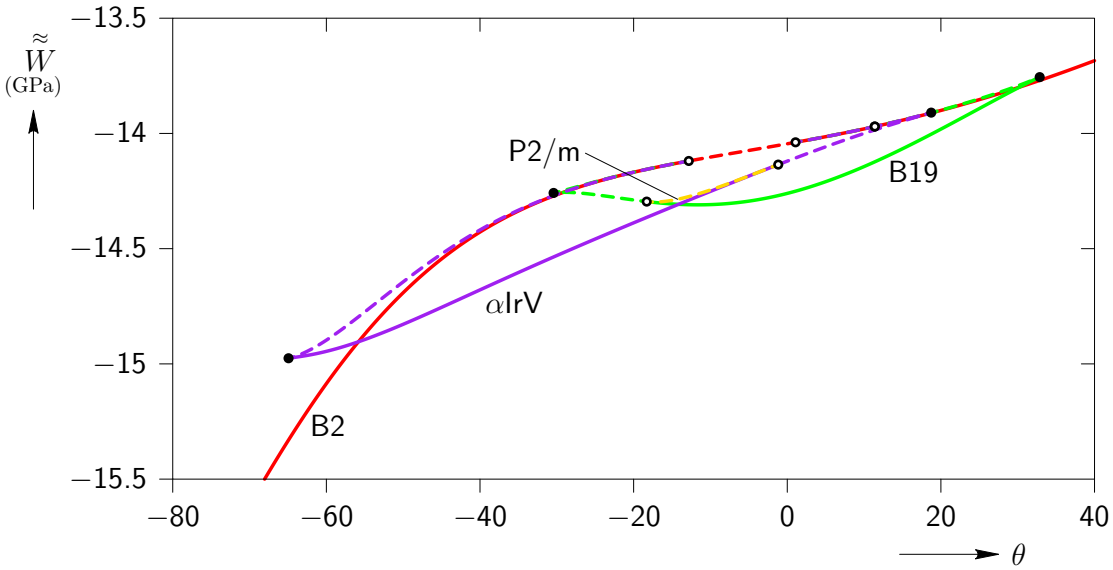

Fig. 8 Variation of Homogenized Continuum free energy density $\approx\!\approx W$ for B2, B19, αIrV, and P2/m crystal structures with respect to non-dimensional temperature θ.

The introduction of the temperature-dependent parameter $B(\theta)$ provides a mechanism by which the model may reduce its free energy as the temperature increases at constant configuration. A negative value of B_θ is needed to obtain positive entropies and heat capacities, and thus the effective potential bonds are expected to soften with θ, i.e., $B(\theta)$ decreases with increasing temperature.

The fitting procedure of Section 5 remains unchanged, but in addition, the heat capacity C_p at the reference temperature for Au, Cd, and the B2 AuCd alloy are matched by the choice of the new parameters B_θ^{aa}, B_θ^{bb}, and B_θ^{ab} respectively. Table 7 gives the experimental values for the heat capacities used for fitting. Note, due to the temperature dependence of $B(\theta)$, new values of $r_\theta^{aa}, r_\theta^{bb}$, and r_θ^{ab} must also be determined in order to ensure that the model matches the experimental thermal expansion values.

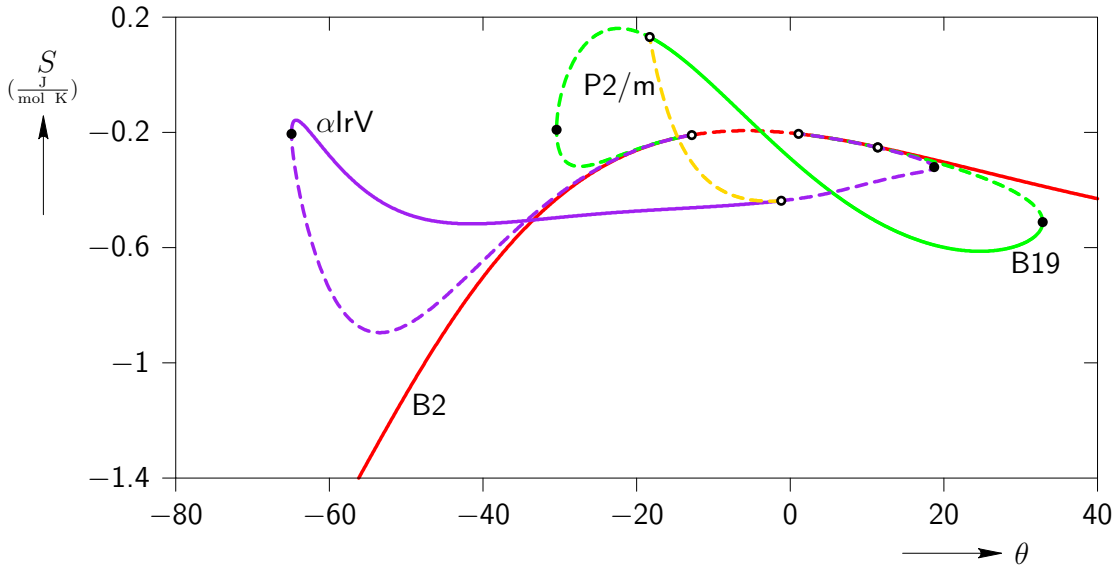

Fig. 9 Variation of entropy per mole S for B2, B19, αIrV, and P2/m crystal structures with respect to non-dimensional temperature θ.

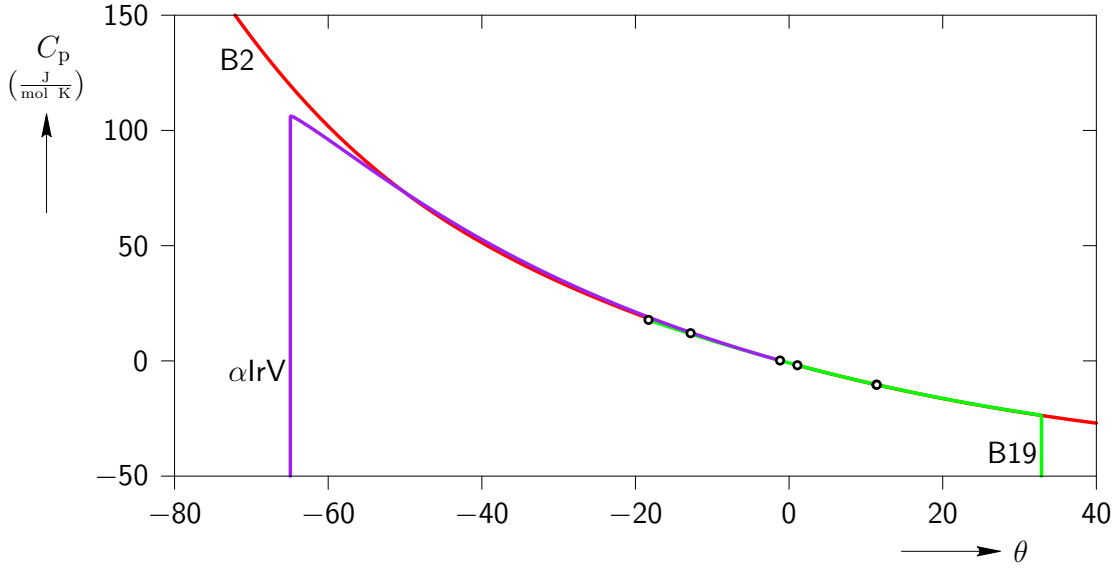

Fig. 10 Variation of heat capacity per mole at constant pressure C_p for stable path segments of the B2, B19, and αIrV crystal structures with respect to non-dimensional temperature θ.

Using the definition of C_p from Eq. (17), and a trial and error approach, the fitted parameters given in Table 8 are obtained.

Thus, the potentials of Eq. (24) along with the parameters given in Table 8 fully define a new EIP model for Au-47.5at%Cd. This model matches the B2 lattice parameter, instantaneous bulk modulus, linear thermal expansion coefficient, and heat capacity of B2 AuCd at the experimental transformation temperature (reference temperature, $\theta = 1$). Additionally, the B2 structure is unstable for temperatures below $\theta = 1$ and stable (CB and phonon) for temperatures greater than $\theta = 1$.

Figure 11 shows the variation of cohesive energy, linear thermal expansion coefficient, lattice parameter, entropy per mole, instantaneous bulk modulus, and heat capacity per mole at constant pressure of FCC Au with respect to non-dimensional temperature θ. Again, it is recognized that negative values

of θ are not physical, but the full diagrams are presented for consistency with figures of Section 8 and so that the model's complete range of behavior is illustrated. The plus signs show the experimental values given in Table 1 and Table 7. The cohesive energy increases with θ. The linear thermal expansion coefficient decreases with θ. This is in contradiction to general experimental observation (*Villars et al.*, 1985). The lattice parameter increases as θ is increased but starts decreasing for temperatures above about $\theta = 1.8$. Again, this is in contradiction with general experimental observation (*Villars et al.*, 1985). The instantaneous bulk modulus decreases as θ increases and the entropy per mole increases as θ increases. The heat capacity per mole at constant pressure decreases as θ increases for negative values of θ. However, for positive values of θ, it increases with θ which satisfies the general thermodynamic principles.

Figure 12 shows values for HCP Cd of the cohesive energy, in-plane linear thermal expansion coefficient, close-packed plane lattice parameter, entropy per mole, instantaneous bulk modulus, and heat capacity per mole at constant pressure. The plus sign in each plot shows the experimental values given in Table 3 and Table 7. In this case, the cohesive energy rapidly increases as θ increases for higher temperatures. The in-plane linear thermal expansion coefficient decreases rapidly with increasing θ at higher temperatures. The lattice parameter increases for low temperatures but starts decreasing for temperatures above $\theta = 1.8$. This is in contradiction with the experimental observation. The instantaneous bulk modulus decreases as θ increases and the entropy per mole increases with θ. The heat capacity per mole at constant pressure decreases as θ increases for negative values of θ, but increases with θ for positive values of θ.

Figure 13 shows the variation of cohesive energy, linear thermal expansion coefficient, lattice parameter, entropy per mole, instantaneous bulk modulus, and heat capacity per mole at constant pressure

Material	Heat capacity, C_p ($\frac{\mathrm{J}}{\mathrm{mol\ K}}$)
Au	25.5117308
Cd	26.2962308
Au-47.5at%Cd	26.3181507

Table 7 Experimental values of heat capacity per mole at constant pressure (C_p) of pure Au, pure Cd, and B2 Au-47.5at%Cd at 323 K (*Wallace*, 1998; *McGilip*, 1987).

Model 2	
Potential parameter	Value
A^{aa}	0.4754131760 eV
B^{aa}_ref	4.7765863800
B^{aa}_θ	−0.3512000000
r^{aa}_ref	3.0284951200 Å
r^{aa}_θ	0.0602367679 Å
A^{bb}	0.1450200350 eV
B^{bb}_ref	4.8068349900
B^{bb}_θ	−0.6543000000
r^{bb}_ref	3.1179265800 Å
r^{bb}_θ	0.1066030280 Å
A^{ab}	0.1426239530 eV
B^{ab}_ref	6.0000000000
B^{ab}_θ	−0.9648000000
r^{ab}_ref	3.0855868000 Å
r^{ab}_θ	0.0979112472 Å

Table 8 Fitted parameters for the Au-47.5at%Cd Morse EIP model of Eq. (24).

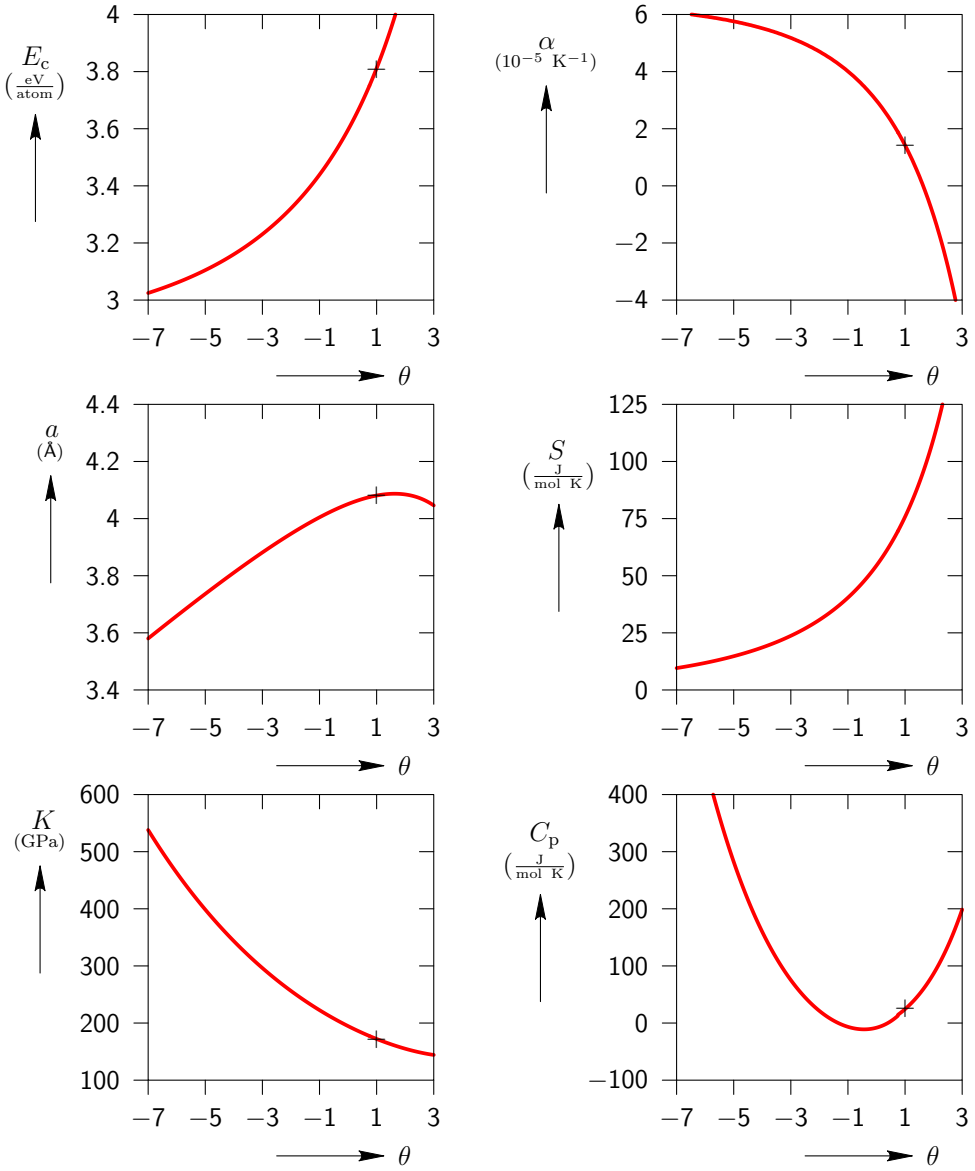

Fig. 11 Variation of cohesive energy E_c, linear thermal expansion coefficient α, lattice parameter a, entropy per mole S, instantaneous bulk modulus K, and heat capacity per mole at constant pressure C_p of FCC Au vs. non-dimensional temperature θ for the parameters in Table 8. Plus signs identify the corresponding experimental values at the reference temperature $\theta = 1$.

of B2 AuCd. The plus sign in each plot shows the corresponding experimental value given in Table 5 or Table 7. Note that it was not possible to match the experimental cohesive energy E_c at the reference temperature. The cohesive energy increases with θ for positive θ. The linear thermal expansion coefficient decreases as θ increases which is in contradiction with experimental results. For low values of θ, the lattice parameter increases with θ, but around $\theta = 1.8$ it starts decreasing. This is also in contradiction with experimental observations. The instantaneous bulk modulus decreases as θ increases and entropy per mole increases as θ increases. The heat capacity per mole at constant pressure decreases as θ increases for negative values of θ but increases for positive values of θ, in agreement with thermodynamic principles.

The unphysical negative thermal expansion coefficient found for this model is certainly undesirable. We believe that this aspect of the model's behavior could be rectified by the use of a more general

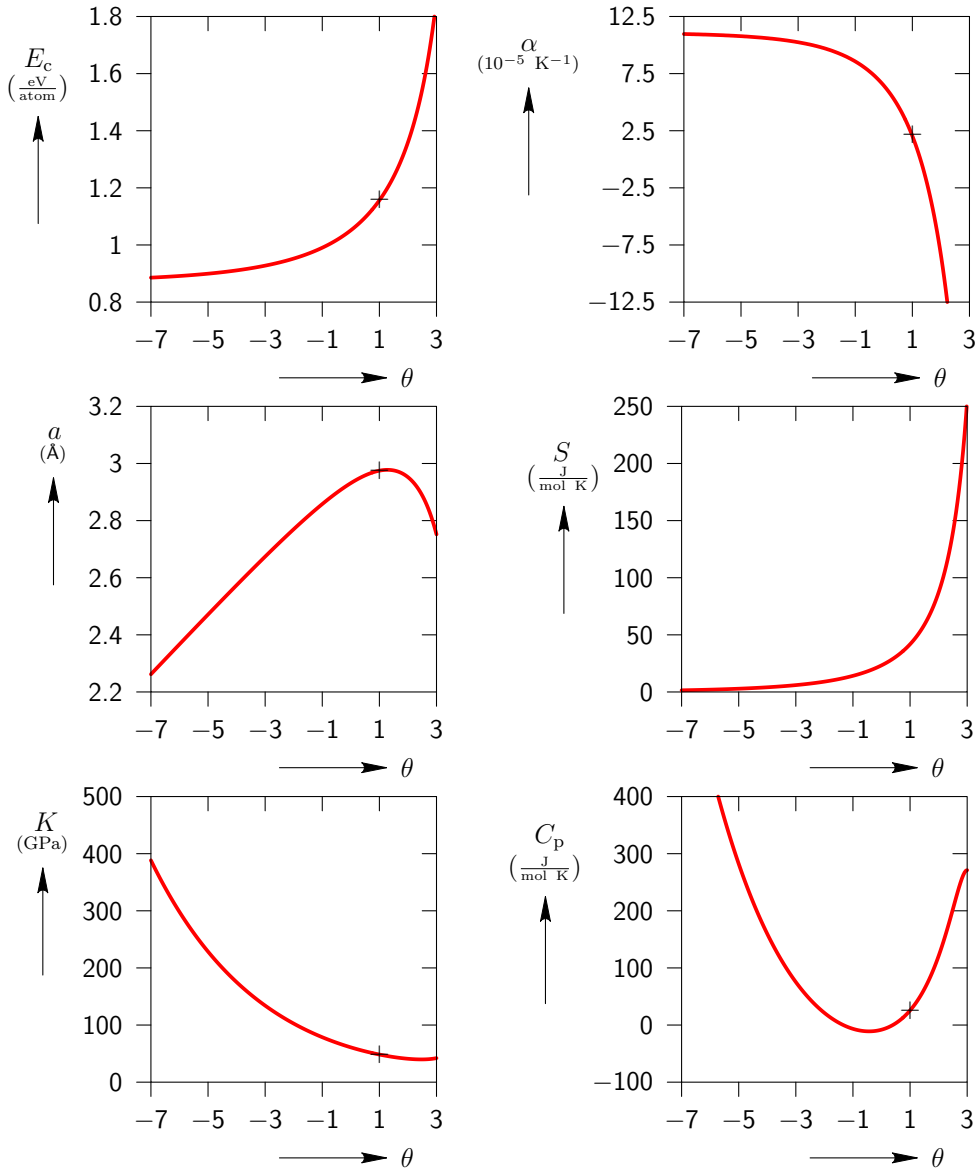

Fig. 12 Variation of cohesive energy E_c, in-plane linear thermal expansion coefficient α, close-packed plane lattice parameter a, entropy per mole S, instantaneous bulk modulus K, and heat capacity per mole at constant pressure C_p of HCP Cd vs. non-dimensional temperature θ for the parameters in Table 8. Plus signs identify the corresponding experimental values at the reference temperature $\theta = 1$.

EIP model with more complicated temperature dependence of the potential parameters. However, the development of such a model is not pursued in this work.

8 Temperature-induced MTs associated with Model 2

A stress-free bifurcation diagram is generated for Model 2 in order to evaluate its ability to correctly predict the B2 to B19 phase transformation found in Au-47.5at%Cd. Figure 14 displays the results by plotting the maximum principal stretch λ_3 vs. non-dimensional temperature θ. The B2 austenite phase (red line) is stable at higher temperatures and becomes unstable as the temperature is decreased with bifurcation at $\theta = 1$ (T_{ref}=323 K). The B2 phase is predicted to re-stabilize for temperatures below $\theta = -4.48$. However, if one restricts attention to positive temperatures (which have physical

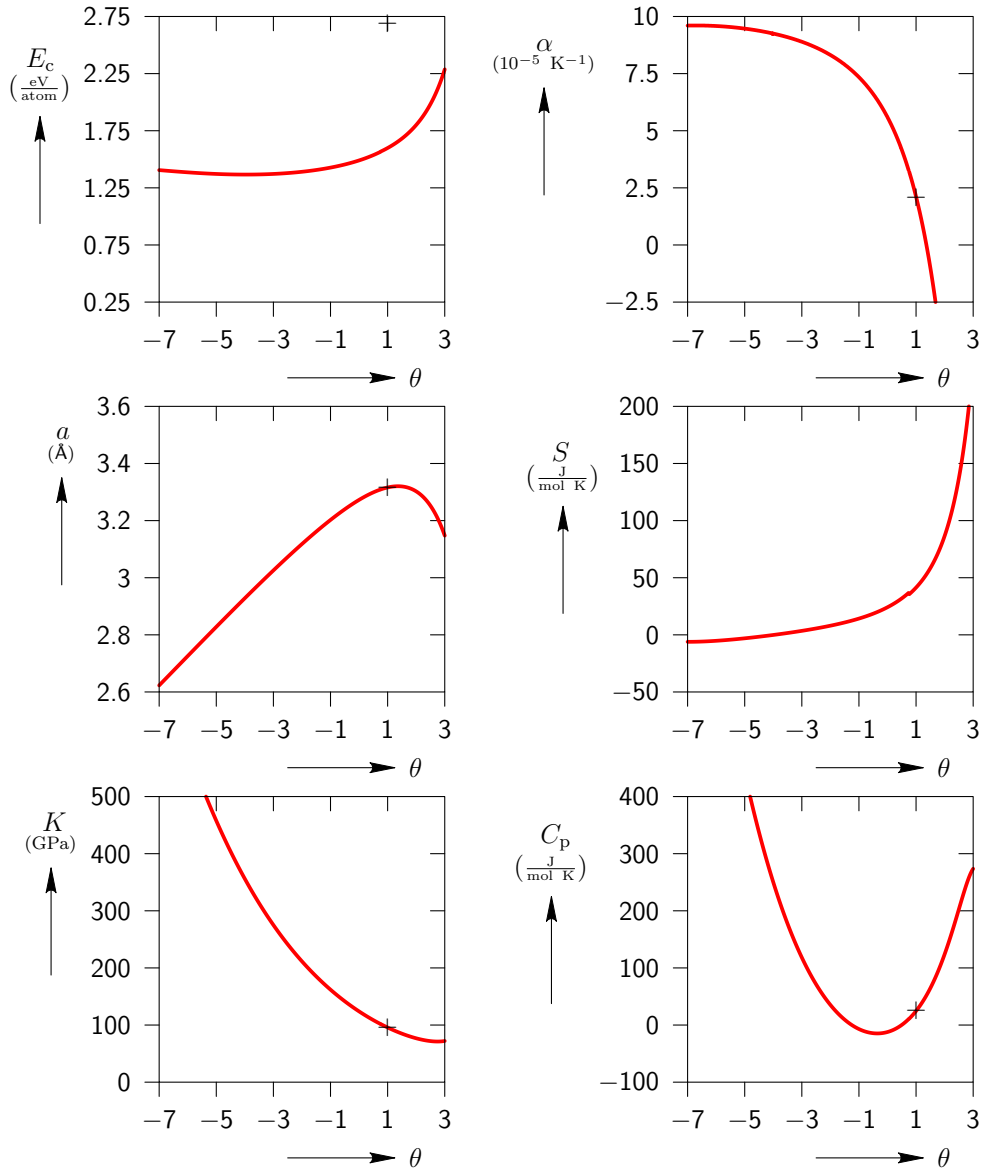

Fig. 13 Variation of cohesive energy E_c, linear thermal expansion coefficient α, lattice parameter a, entropy per mole S, instantaneous bulk modulus K, and heat capacity per mole at constant pressure C_p of B2 Au-47.5at%Cd vs. non-dimensional temperature θ for the parameters in Table 8. Plus signs identify the corresponding experimental values at the reference temperature $\theta = 1$.

significance) a reasonable correspondence with experiments can be identified. A set of B19 and αIrV orthorhombic equilibrium paths emerge from the bifurcation point at $\theta = 1$. The B19 equilibrium path (green line) is initially unstable as it emerges from the bifurcation point, but becomes stable at a turning point near $\theta = 2.18$. It continues to be stable until it encounters the bifurcation point at $\theta = -3.96$. Eventually, the B19 path reconnects with the original B2 path at a bifurcation point near $\theta = -4.48$. Similarly, the αIrV equilibrium path (purple line) is initially unstable but becomes stable near $\theta = 2.18$. It continues to be stable until $\theta = 1.24$ where it encounters a bifurcation point. The αIrV path becomes stable once again at the bifurcation point near $\theta = -2.24$ and it remains stable until it encounters a turning point at $\theta = -6.76$. Finally, it reconnects with the B2 path at the same bifurcation point as the B19 path. It is also observed that unstable paths of a monoclinic structure with space group P2/m (yellow lines) connect the B19 path to the αIrV path through their respective bifurcation points. On further exploration, it is observed that an unstable $L1_0$ path (blue line) emerges

from a second bifurcation point on the B2 path at $\theta = 0.46$. It becomes stable near $\theta = 2$ and continues to be stable until $\theta = -5.03$. Two additional unstable paths of the B19 and αIrV phases are also found that connect the two secondary bifurcation points on the $L1_0$ path at $\theta = 0.65$ and $\theta = -4.19$.

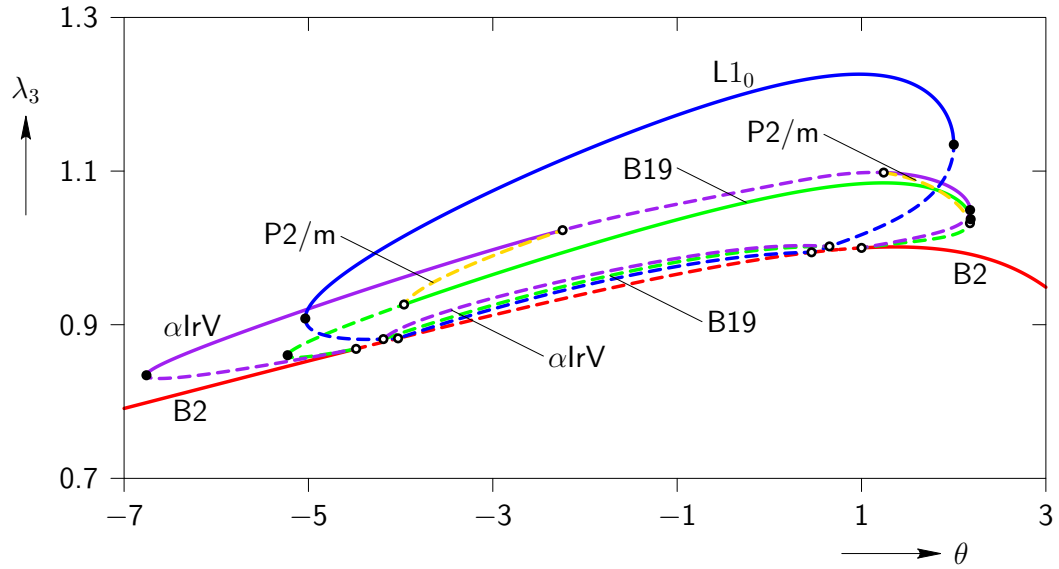

Fig. 14 Variation of λ_3 (largest eigenvalue of $\mathbf{U}$) of B2, B19, αIrV, P2/m, and $L1_0$ crystal structures of Au-47.5at%Cd with respect to non-dimensional temperature θ.

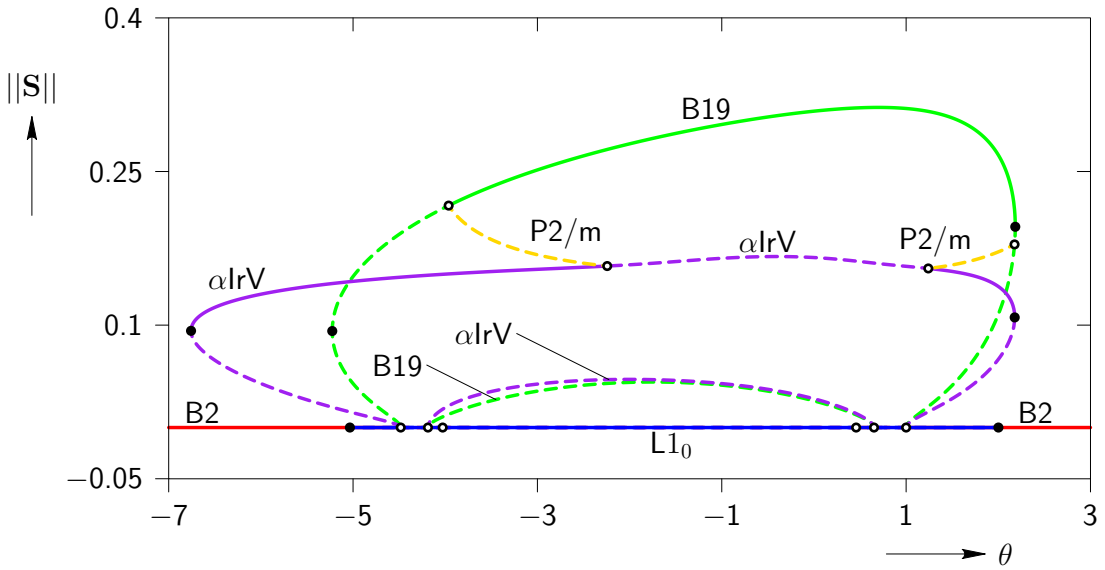

Fig. 15 Variation of $||\mathbf{S}||$ of B2, B19, αIrV, P2/m, and $L1_0$ crystal structures of Au-47.5at%Cd with respect to non-dimensional temperature θ.

Figure 15 plots the variation of the norm of the internal atomic shifts $||\mathbf{S}||$ with respect to the non-dimensional temperature θ. Here the norm is defined as $||\mathbf{S}|| = (||\mathbf{S}[1]||^2 + ||\mathbf{S}[2]||^2 + ||\mathbf{S}[3]||^2)^{\frac{1}{2}}$. In this figure the $L1_0$ path (for which $||\mathbf{S}|| = 0$) falls directly over the B2 path.

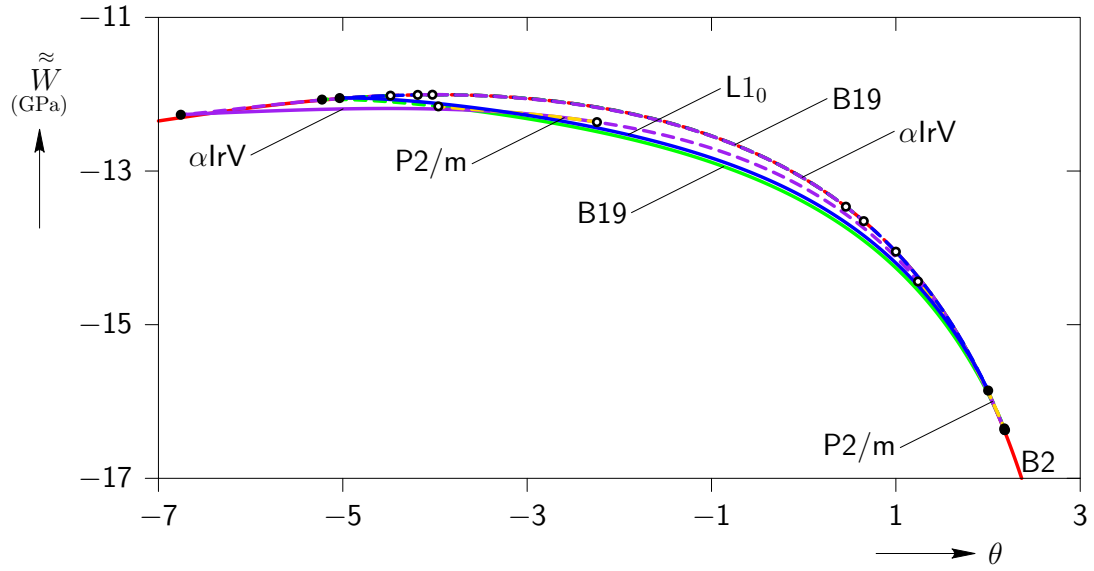

Fig. 16 Variation of free energy density $\approx\!\!\approx W$ of B2, B19, αIrV, P2/m, and L1$_0$ crystal structures of Au-47.5at%Cd with respect to non-dimensional temperature θ.

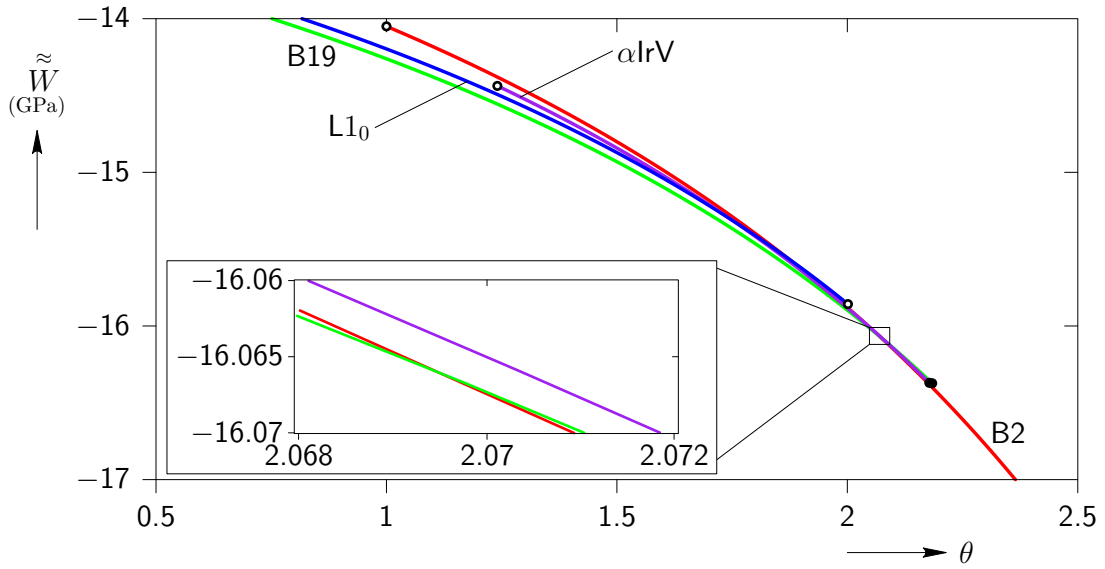

Fig. 17 Variation of free energy density $\approx\!\!\approx W$ of stable path segments for the B2, B19, αIrV, P2/m, and L1$_0$ crystal structures of Au-47.5at%Cd with respect to non-dimensional temperature θ.

The variation of the HC free energy density $\approx\!\!\approx W$ with respect to the non-dimensional temperature θ is plotted in Fig. 16. For non-dimensional temperatures above $\theta = -3$ the slope and curvature of all stress-free equilibrium paths are found to be negative. This indicates that the entropy and heat capacity at constant pressure are positive, as required by equilibrium thermodynamics. For temperatures below $\theta = -3$, this is not the case. However, this is not a problem since negative temperatures do not have physical significance. At this point, we restrict our attention to a positive temperature range of $\theta = 0.5$ to $\theta = 2.5$ and consider the variation of the HC free energy density $\approx\!\!\approx W$, unit cell volume V, cohesive energy E_c, instantaneous bulk modulus K, entropy per mole S, and heat capacity per mole at constant pressure C_p of the stable path segments with respect to non-dimensional temperature θ.

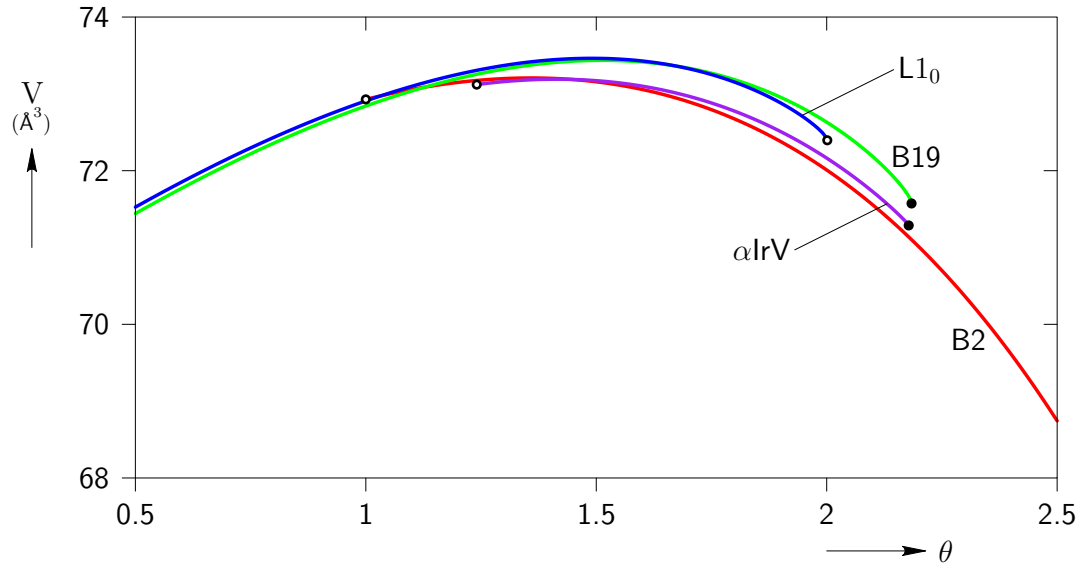

Fig. 18 Variation of unit cell volume of the B2, B19, αIrV, and L1$_0$ crystal structures for Au-47.5at%Cd with respect to non-dimensional temperature θ.

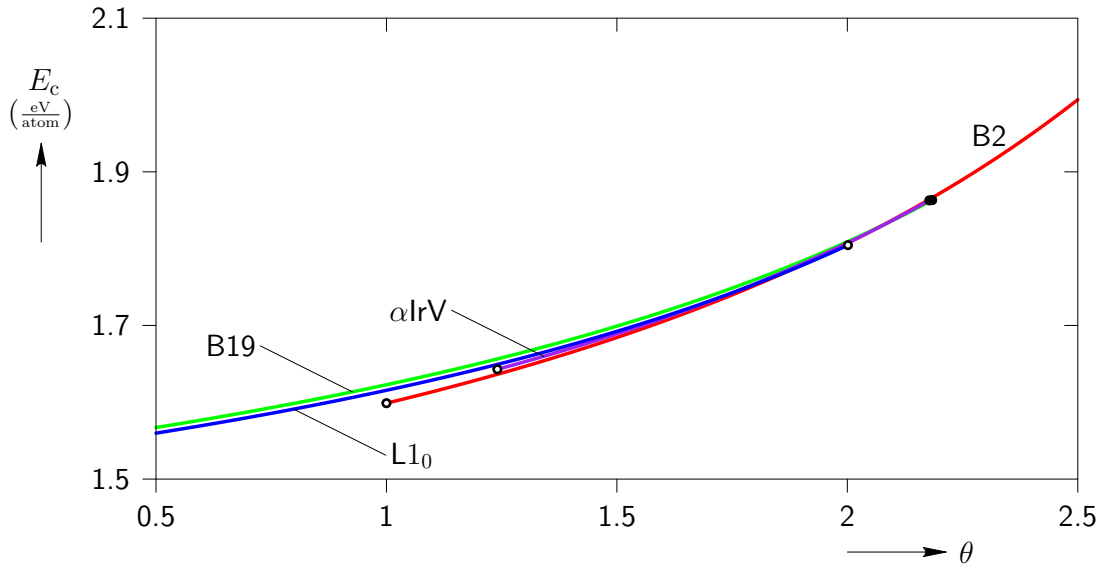

Fig. 19 Variation of cohesive energy E_c of the B2, B19, αIrV, and L1$_0$ crystal structures for Au-47.5at%Cd with respect to non-dimensional temperature θ.

Figure 17 displays the variation of $\widetilde{\widetilde{W}}$ of the B2, B19, αIrV, and L1$_0$ stable phases with respect to θ. At high temperatures the B2 crystal is the only stable phase. Figure 18 displays the variation of unit cell volume with respect to non-dimensional temperature θ. The unit cell volume of all stable phases are nearly equal which shows that any MTs predicted by this model will result in a volume change of less than 1%. At low temperatures, the volume increases as temperature is increased which is in coincidence with general experimental observations, but it starts decreasing for temperatures above around $\theta = 1.4$. This is not the behavior that is observed experimentally. However, if one restricts consideration to values of θ below 1.4, the model is in reasonable agreement with the general experimental observations. Figure 19 displays the variation of cohesive energy with respect to the non-dimensional temperature θ. The cohesive energy is found to increase with temperature for all phases. Figure 20 displays the

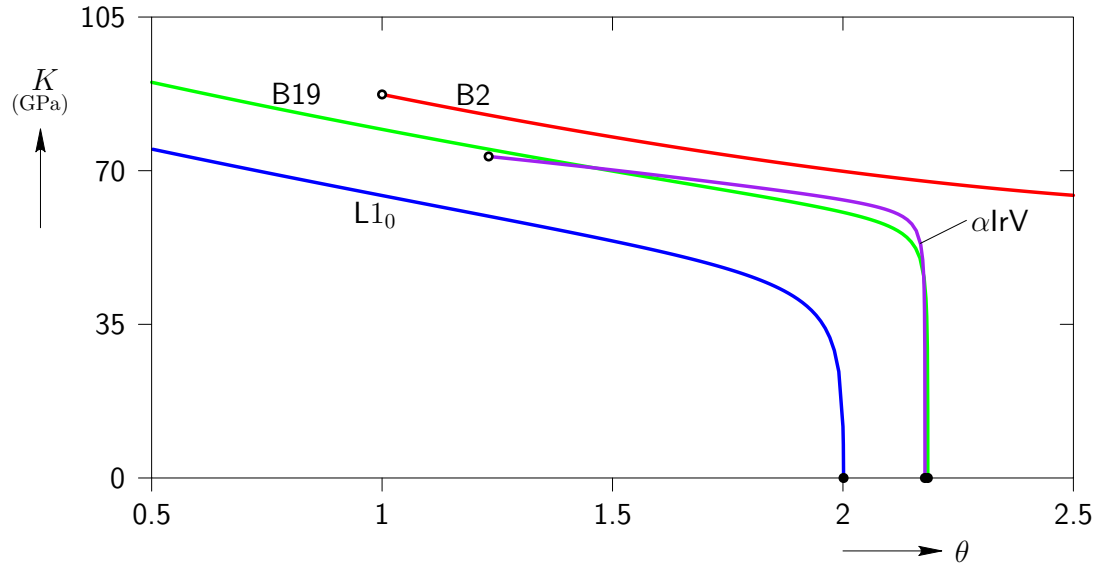

Fig. 20 Variation of instantaneous bulk modulus K of the B2, B19, αIrV, and $L1_0$ crystal structures for Au-47.5at%Cd with respect to non-dimensional temperature θ.

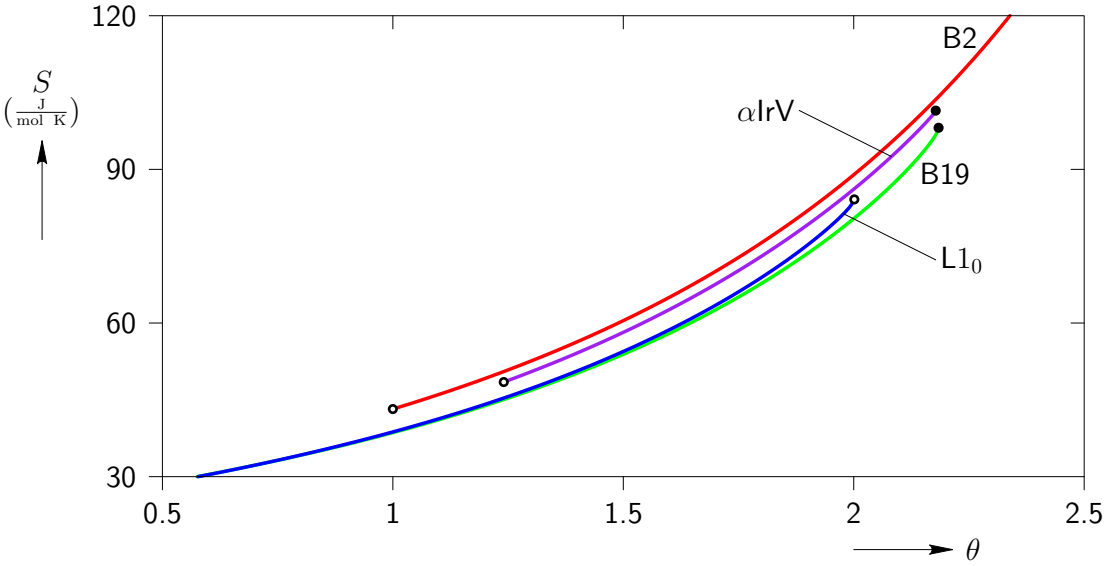

Fig. 21 Variation of entropy S of the B2, B19, αIrV, and $L1_0$ crystal structures for Au-47.5at%Cd with respect to non-dimensional temperature θ.

variation of instantaneous bulk modulus with respect to non-dimensional temperature θ. Figures 21 and 22 display the variation of entropy and heat capacity at constant pressure, respectively, with respect to non-dimensional temperature θ. In general, entropy and heat capacity are found to increase with temperature. This is in general agreement with thermodynamic theory. Note that both entropy and heat capacity at constant pressure are positive which is not the case in Model 1.

Returning to Fig. 17, it is observed that upon decreasing temperature the B2 phase becomes metastable at $\theta = 2.069$ (with the B19 phase having lower free energy for higher temperatures) and finally loses stability at $\theta = 1$. At this temperature the only stable phases are B19 and $L1_0$. However, B19 is the stable phase with minimum free energy. Thus, a transformation from B2 to B19 can be expected. For lower temperatures the B19 phase continues to be the stable phase with minimum

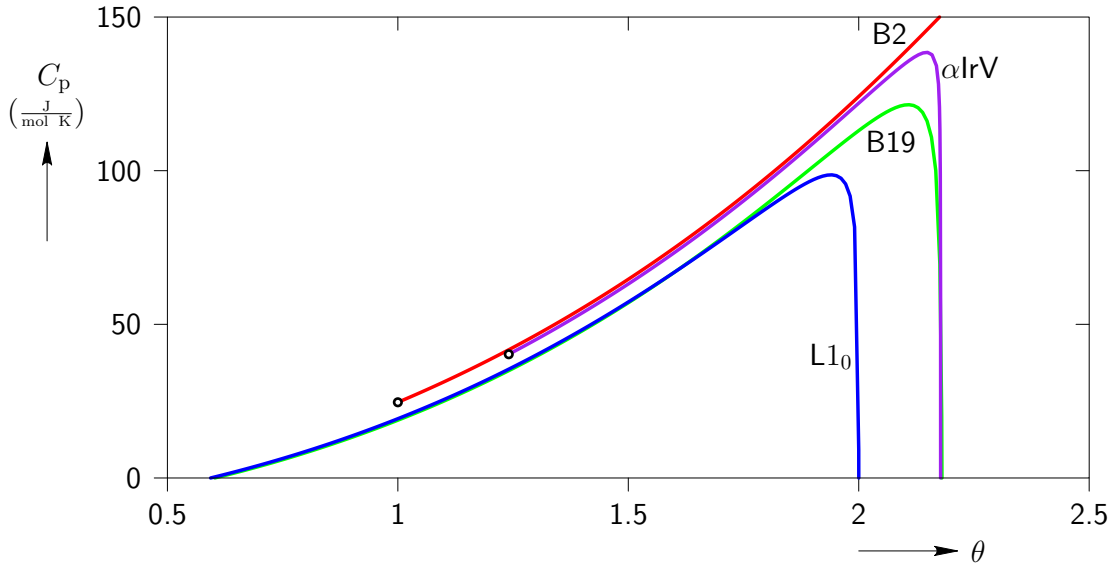

Fig. 22 Variation of heat capacity at constant pressure C_p of the B2, B19, αIrV, and $L1_0$ crystal structures for Au-47.5at%Cd with respect to non-dimensional temperature θ.

free energy. In the case of increasing temperature, the orthorhombic B19 structure has the global minimum free energy until $\theta = 2.069$ where it becomes metastable with respect to the B2 phase. It loses stability soon afterward at $\theta = 2.19$ where it ceases to exist for higher temperatures. Thus, a hysteretic martensitic transformation between the B2 and B19 structures is predicted. Ideally, one should verify that no other equilibrium crystal structures exist with lower energy. This would ensure that the minimum energy phases shown in Fig. 17 capture the model's ground state phase at any given temperature. However, this theoretically infinite investigation is not pursued in this work.

At the transformation temperature, 323 K (*Zirinsky*, 1956), the transformation stretch is

$$\mathbf{U}^* = \begin{pmatrix} 1.05451615 & 0.02919474 & 0 \\ 0.02919474 & 1.05451615 & 0 \\ 0 & 0 & 0.899214532 \end{pmatrix}, \tag{25}$$

which is same as that found in Section 6. This is because the models of Section 5 (Model 1) and Section 7 (Model 2) coincide when $\theta = 1$. The latent heat ($\Delta\overset{\approx}{W} + T\Delta S$) associated with the B2 to B19 transformation at $\theta = 1$ is calculated as $-557.41 - 218.14 = -775.55\ \frac{cal}{mol}$ (negative values correspond to exothermic transition) which is within a factor of 10 of the experimental value for the latent heat of transformation from B2 to B19 which is $-88\ \frac{cal}{mol}$ (*Nakanishi et al.*, 1973). In contrast to Model 1, Model 2 is more accurate in two important ways. First, the current model has positive entropy and heat capacity (at least for positive temperatures), as required by equilibrium thermodynamics. Second, the temperature range over which the B19 phase is stable is more in line with what is observed experimentally.

Thus, it is found that the current Morse EIP model for Au-47.5at%Cd is able to match the lattice parameter, instantaneous bulk modulus, and stability range of the B2 austenite phase as well as the austenite's linear thermal expansion coefficient and its heat capacity at constant pressure at $\theta = 1$. Further, the model predicts the existence of a temperature-induced hysteretic B2 to B19 martensitic phase transformation, and the transformation stretch tensor is predicted with reasonable accuracy. Finally, the latent heat of transformation and the size of the temperature hysteresis are predicted to be within an order of magnitude.

9 Discussion

An Effective Interaction Potential (EIP) model is developed to study the properties of crystalline materials. In this model, effective pair potentials are used for the material's atomic interactions and the deformations of the crystal are described by Cauchy-Born (CB) kinematics. The crystal's free energy density and equilibrium equations are formulated and stability criteria (both CB and phonon) are used to evaluate the material's stability at any equilibrium configuration. This general model is then applied to study the properties of the Shape Memory Alloy (SMA) Au-47.5at%Cd.

A first model uses temperature-dependent Morse pair potentials with the pair equilibrium spacing taken as a linear function of temperature and all other parameters independent of temperature. The adjustable parameters in each potential are fit by matching the Au-47.5at%Cd experimental values of lattice parameter, instantaneous bulk modulus, cohesive energy, and linear thermal expansion coefficient at the transformation temperature. The model is evaluated by calculating its stress-free equilibrium bifurcation diagram. This diagram identifies the existence of stable B2 cubic, B19 orthorhombic, and αIrV orthorhombic phases. From the plot of maximum principal stretch vs. non-dimensional temperature it is observed that the B19 phase is the only stable phase that exists below the transformation temperature ($\theta = 1$) where the B2 phase become unstable. This indicates the possibility of a Martensitic Transformation (MT) between the B2 and B19 structures. The associated transformation stretch tensor is calculated and found to be in reasonable agreement with the corresponding experimental value. However, a plot of the stress-free Homogenized Continuum (HC) free energy density with respect to temperature reveals a couple of problems with this model. First, the B19 phase is found to be stable for a wide range of temperatures which implies too large of a temperature hysteresis for the $B2 \leftrightarrow B19$ MT. Second, the model predicts negative values of both entropy and heat capacity at constant pressure which violate the basic laws of equilibrium thermodynamics for a stable material.

Therefore, a second model is developed using a more general form of the Morse EIP model that is capable of addressing these short comings. In this model the temperature dependence is extended to include a linear temperature dependence of the bond stiffness parameter. The fitting procedure of the first model is used again, and in addition, the heat capacity at constant pressure of Au, Cd, and B2 AuCd are matched at the reference temperature. A stress-free bifurcation diagram is generated to evaluate the new model's ability to correctly predict the MT between the B2 and B19 structures. From the plot of the maximum principal stretch vs. non-dimensional temperature it is observed that a $B2 \leftrightarrow B19$ MT occurs with a reasonable temperature hysteresis. The transformation stretch is found to be in reasonable agreement with the experimental value. Further, it is found that the current model is able to capture the (approximately) volume preserving nature of the martensitic transformation in AuCd. However, the model predicts a decrease in unit cell volume as temperature increases which is in contradiction to experimental observations. It is also found that the model predicts the latent heat of transformation and size of temperature hysteresis to within an order of magnitude. We believe that a more general EIP model would be capable of correcting the negative thermal expansion and improving the prediction of latent heat and thermal hysteresis. However, the development of this model is left to future work.

Thus, the final Morse EIP model (Model 2) is capable of matching lattice parameter, instantaneous bulk modulus, cohesive energy, linear thermal expansion coefficient, and heat capacity at the reference temperature. Further, the model predicts the existence of a B2 to B19 martensitic phase transformation with properties that are in agreement with experimental observations. It should be noted that the fitting procedure used in the model's development did not include any data associated with the B19 martensite phase of the material.

Based on the above positive results, it is believed that EIP models have the potential for accurately capturing the entire range of SMA behavior. These EIP models are computationally inexpensive when compared to Molecular Dynamics, Monté Carlo, and Density Functional Theory models. Thus, EIP models are an appealing accurate and computationally efficient alternative to more traditional simulation methodologies when one is interested in performing large scale simulations (such as the formation of complicated microstructures, or the interaction of a crack tip with the phase transformation) for materials that exhibit MTs including SMAs.

Acknowledgements
The authors would like to thank Ellad B. Tadmor and Traian Dumitrica for helpful comments and suggestions.

This work has been supported by the National Science Foundation CAREER Grant CMMI-0746628 (Dr. Shih-Chi Liu, Program Director); by The University of Minnesota Grant-In-Aid of Research, Artistry and Scholarship Program (GIA); and by The University of Minnesota Supercomputing Institute.

References

K. Bhattacharya. *Microstructure of Martensite: Why It Forms and How It Gives Rise to the Shape-Memory Effect*. Oxford University Press, 2003.

L. C. Brinson. One dimensional constitutive behavior of shape memory alloys: thermomechanical derivation with non-constant material functions. *Journal of Intelligent Material Systems and Structures*, 4(2):229–242, 1993.

L. C. Brinson and M. S. Huang. Simplifications and comparisons of shape memory alloy constitutive models. *Journal of Intelligent Material Systems and Structures*, 7:108–114, 1996.

A. Bystrom and K. E. Almin. X-ray investigation of AuCd alloys rich in Au. *Acta Chemica Scandinavica*, 1(1):76–89, 1947.

L. C. Chang and T. A. Read. Plastic deformation and diffusionless phase changes in metals - the AuCd β-phase. *Transactions of the American Institute of Mining and Metallurgical Engineers*, 191(1):47–52, 1951.

R. S. Elliott. Multiscale bifurcation and stability of multilattices. *Journal of Computer-aided Materials Design*, 2008. doi:10.1007/s10820-007-9075-8.

R. S. Elliott, J. A. Shaw, and N. Triantafyllidis. Stability of pressure-dependent, thermally-induced displacive transformations in bi-atomic crystals. *International Journal of Solids and Structures*, 39(13-14):3845–3856, 2002a.

R. S. Elliott, J. A. Shaw, and N. Triantafyllidis. Stability of thermally-induced martensitic transformations in bi-atomic crystals. *Journal of the Mechanics and Physics of Solids*, 50(11):2463–2493, 2002b.

R. S. Elliott, N. Triantafyllidis, and J. A. Shaw. Stability of crystalline solids–I: Continuum and atomic-lattice considerations. *Journal of the Mechanics and Physics of Solids*, 54(1):161–192, 2006a.

R. S. Elliott, N. Triantafyllidis, and J. A. Shaw. Stability of crystalline solids–II: Application to temperature-induced martensitic phase transformations in a bi-atomic crystal. *Journal of the Mechanics and Physics of Solids*, 54(1):193–232, 2006b.

P. Entel, K. Kadau, R. Meyer, H. C. Herper, M. Schroter, and E. Hoffmann. Large-scale molecular-dynamics simulations of martensitic nucleation and shape-memory effects in transition metal alloys. *Phase Transitions*, 65:79–108, 1999.

P. Entel, R. Meyer, and K. Kadau. Molecular dynamics simulations of martensitic transitions. *Philosophical Magazine B-Physics of Condensed Matter Statistical Mechanics Electronic Optical and Magnetic Properties*, 80(2):183–194, 2000.

L. Fast, J. M. Wills, B. Johansson, and O. Eriksson. Elastic-constants of hexagonal transition-metals - theory. *Physics Review B*, 51(24):17431–17438, 1995.

C. W. Garland and J. Silverman. Elastic constants of Cadmium from 4.2 K to 300 K. *Physical Review*, 119(4):1218–1222, 1960.

L. A. Girifalco and V. G. Weizer. Application of the Morse potential function to cubic metals. *Physical Review*, 114(3):687–690, 1959.

B. C. Goo and C. Lexcellent. Micromechanics based modeling of two-way memory effect of a single crystalline shape memory alloy. *Acta Metallurgica*, 45:727–737, 1997.

M. Grujicic and P. Dang. Computer simulation of martensitic transformation in Fe-Ni face-centered cubic alloys. *Materials Science & Engineering A*, 201:194–204, 1995.

V. S. Guthikonda. *Effective Morse interaction potentials for modeling lattice-level instabilities in shape memory alloys*. MS thesis, Univeristy of Minnesota, Minneapolis, MN 55455, 2007.

V. S. Guthikonda and R. S. Elliott. Stability and elastic properties of the stress-free B2 (CsCl-type) crystal for the Morse pair potential model. *Journal of Elasticity*, 2008. In press.

V. S. R. Guthikonda, M. K. Kiran, S. M. Sivakumar, and A. R. Srinivasa. On smeared and micromechanical approaches to modeling martensitic transformations in SMA. *Nonlinear Analysis: Real World Applications*, 9:990–1011, 2008.

K. Huang and M. Born. *Dynamical Theory of Crystal Lattices*. Oxford University Press, 1962.

M. S. Huang and L. C. Brinson. A multivariant model for single crystal shape memory alloys. *Journal of the Mechanics and Physics of Solids*, 46:1379–1409, 1998.

X. Huang, C. Bungarao, V. Godlevsky, and K. M. Rabe. Lattice instabilities of cubic NiTi from first principles. *Physical Review B-Condensed Matter*, 65(1):1–5, 2002.

X. Huang, K. M. Rabe, and G. J. Ackland. Crystal structures and shape-memory behavior of NiTi. *Nature Materials*, 2(5):307–311, 2003.

H. Ishida and Y. Hiwatari. MD simulation of martensitc transformations in TiNi alloys with MEAM. *Molecular Simulation*, 33:459–461, 2007.

Y. Ivshin and T. J. Pence. A constitutive model for hysteretic phase transition behavior. *International Journal of Engineering Science*, 32:681–704, 1994.

C. Kittel. *Introduction to Solid State Physics*. Wiley, 2005.

C. Liang and A. Rogers. One-dimensional thermomechanical constitutive relations for shape memory materials. *Journal of Intelligent Material Systems and Structures*, 1(2):207–234, 1990.

Z. K. Lu and G. J. Weng. Martensitic transformations and stress-strain relations of shape-memory alloys. *Journal of the Mechanics of Physics of Solids*, 45:1905–1928, 1997.

J. F. McGilip. Alloying and entropy effects in predicting metal/compound-semiconductor interface reactivity. *J. Mater. Res.*, 2(4):516–523, 1987.

R. Meyer and P. Entel. Martensite-austenite transition and phonon dispersion curves of $Fe_{1-x}Ni_x$ studied by molecular-dynamics simulations. *Physical Review B*, 57(9):5140–5147, 1998.

N. Nakanishi, T. Mori, S. Miura, Y. Murakami, and S. Kachi. Pseudoelasticity in Au-Cd thermoelastic martensite. *Philosophical Magazine*, 28:277–292, 1973.

J. R. Neighbours and G. A. Alers. Elastic constants of Silver and Gold. *Physical Review*, 111(3):707–712, 1958.

T. Ohba, Y. Emura, S. Miyazaki, and K. Otsuka. Crystal structure of γ_2' martensite in Au-47.5%Cd alloy. *Materials Transactions JIM*, 31(1):12–17, 1990.

A. Olander. The crystal structure of AuCd. *Zeitschrift Fur Kristallographie*, 83(1/2):145–148, 1932.

S. Ozgen and O. Adiguzel. Molecular dynamics simulations of diffusionless phase transformation in quenched NiAl alloy model. *Journal of Physics and Chemistry of Solids*, 64(3):459–464, 2003.

K. Parlinski, M. Parlinska, and R. Gotthardt. Phonons in austenite and martensite NiTi crystals. *Journal De Physique IV*, 112:635–638, 2003.

K. Parlinski and M. Parlinska-Wojtan. Lattice dynamics of NiTi austenite, martensite, and R phase. *Physical Review B*, 67(064307):1–8, 2002.

E. Patoor, A. Eberhardt, and M. Berveiller. Thermomechanical behavior of shape memory alloys. *Archives of Mechanics*, 40(5-6):775–794, 1988.

E. Patoor, A. Eberhardt, and M. Berveiller. Micromechanical modelling of the shape memory alloys. *Pitman Research Notes in Mathematics Series*, 296:38–54, 1993.

M. Pitteri and G. Zanzotto. *Continuum Models for Phase Transitions and Twinning in Crystals*, volume 19 of *Applied Mathematics*. CRC Press, 2002.

S. Rubini and P. Ballone. Martensitic transformations and phonon localization in Ni-Al alloys by atomistic simulations. *Meccanica*, 30:439–448, 1995.

Y. Shao, P. C. Clapp, and J. A. Rifkin. Molecular dynamics simulation of martensitic transformations in NiAl. *Metallurgical and Materials Transactions A*, 27A:1477–1489, 1996.

J. A. Shaw. A thermomechanical model for a 1-D shape memory alloy wire with propagating instabilities. *International Journal of Solids and Structures*, 39(5):1275–1305, 2002.

Q. P. Sun and K. C. Hwang. Micromechanics modelling for the constitutive behavior of polycrystalline shape memory alloys–I. Derivation of general relations. *Journal of the Mechanics and Physics of Solids*, 41(1):1–17, 1993a.

Q. P. Sun and K. C. Hwang. Micromechanics modelling for the constitutive behavior of polycrystalline shape memory alloys–II. Study of the individual phenomena. *Journal of the Mechanics and Physics of Solids*, 41(1):19–33, 1993b.

K. Tanaka and S. Nagaki. A thermomechanical description of materials with internal variables in the process of phase-transitions. *Ingenieur Archiv*, 51(5):287–299, 1982.

U.S. NRL Center for Computational Materials Science. Crystal lattice structures web page. http://cst-www.nrl.navy.mil/lattice/, 2008.

P. Villars, L. D. Calvert, and W. B. Pearson. *Pearson's handbook of crystallographic data for intermetallic phases*. Metals Park, 1985.

A. Vivet and C. Lexcellent. Micromechanical modelling for tension-compression pseudoelastic behavior of AuCd single crystals. *The European Journal Applied Physics*, 4(2):125–132, 1998.

D. C. Wallace. *Thermodynamics of Crystals*. Courier Dover Publications, 1998.

J. Wang, Y. Wang, R. Schaublin, C. Abromeit, and R. Gotthardt. The effect of point defects on the martensitic phase transformation. *Material Science and Engineering A - Structural Material Properties Microstructure and Processing*, 438:102–108, 2006.

Y. Y. Ye, C. T. Chan, and K. M. Ho. Structural and electronic properties of the martensitic alloys TiNi, TiPd, and TiPt. *Physical Review B*, 56(7):3678–3689, 1997.

S. Zirinsky. The temperature dependence of the elastic constants of Gold-Cadmium alloys. *Acta Metallurgica*, 4(2):164–171, 1956.